PhD Course in Biochemistry

Cycle XXXVII (2021-2024)

Structural and functional characterization of a humanized neutralizing antibody targeting the SARS-CoV-2 Receptor Binding Domain (RBD)

PhD Candidate

Antonella Costanzo

Tutors	**PhD Coordinator**
Dr. Carmelinda Savino	Prof. Maria Luisa Mangoni
Dr. Giuseppe Roscilli	
Prof. Beatrice Vallone	

December 2024

Table of Contents

Introduction

1. Genomic Structure and Pathophysiology of SARS-CoV2

In late December 2019, the novel coronavirus epidemic emerged from China, and on 30 January 2020, the World Health Organization (WHO) declared coronavirus disease 2019 (COVID-19) a pandemic. This virus is closely related to severe acute respiratory syndrome coronavirus (SARS-CoV), first emerged in 2003 and it has been named SARS-CoV-2 by the Coronavirus Study Group of the International Committee on Taxonomy of Viruses (Nayak et al., 2020).

SARS-CoV-2 is a virus of the *Coronaviridae* family belonging to the *Betacoronavirus* subfamily (Fedry et al., 2021). It has ~29.9 kbp positive-sense single-stranded RNA genome packed in the protein envelope (Saceleanu et al., 2022). The genome consists of 14 functional open reading frames (ORFs) and includes one noncoding region at both ends and multiple regions that encode for non-structural proteins (NSPs), accessory and structural proteins (Kadam et al., 2021). The sixteen NSPs expressed by SARS-CoV2 are involved in disrupting host replication while promoting the synthesis and assembly of new viral products. (Tam et al., 2023). It also encodes for four structural proteins

namely, spike (S), membrane (M) protein, envelope (E), and nucleocapsid (N), that are crucial for virus assembly and infection (C. Bai et al., 2022; Kadam et al., 2021). More in details, N protein is a phosphoprotein that packages the viral genome into a helical ribonucleocapsid and plays a fundamental role during viral self-assembly (Chang et al., 2013). The E protein assists in the assembly and release of virions from host cells by interacting with other structural proteins, like the M protein. It also forms oligomers leading to the viroporins formation, which can alter the ionic balance within the host cell and contribute to viral pathogenesis. The last structural protein is the S protein which is a homotrimer expressed on the viral surface and its role is to mediate the interaction with the angiotensin-converting enzyme 2 (ACE2), highly expressed on the surface of various cell types, including those in the respiratory tract, gastrointestinal tract, kidneys, heart, and other organs (Kadam et al., 2021). After binding to ACE2, the S protein undergoes a series of conformational changes that allow fusion of the viral membrane with the host membrane and entry of the virus into the host cells. SARS-CoV2 can use two pathways to enable virus entry, namely the endocytic pathway and the transmembrane serine protease 2 (TMPRSS2)-mediated surface pathway, which are described below (Walls et al., 2020a).

To a certain extent, the clinical features of COVID-19, such as mild symptoms (dry cough, fever, and sore throat), severe acute respiratory distress syndrome (ARDS) and multi-organ failure (MOF) are due to a combination of the body's immune response to the virus and the direct damage caused by the virus itself. The cellular damage caused by SARS-CoV-2 results primarily from its viral replication and subsequent release from host cells, which triggers a form of inflammatory cell death known as pyroptosis. During pyroptosis, infected cells

undergo lysis, leading to the release of damage-associated molecular patterns (DAMPs). These molecules are recognized by surrounding cells, including epithelial cells, endothelial cells, and alveolar macrophages.

The recognition of DAMPs by neighbouring cells initiates the production of pro-inflammatory cytokines (such as IL-6, IL-1β, and TNF-α) and chemokines (like CCL2 and CXCL10). These signalling molecules play a pivotal role in attracting immune cells, such as monocytes, neutrophils, and T cells, to the site of infection. This recruitment of immune cells exacerbates local inflammation, contributing to tissue damage.

Moreover, the persistent production of cytokines and chemokines leads to a pro-inflammatory feedback loop, amplifying the inflammatory response and potentially causing cytokine storms, a hallmark of severe COVID-19 cases. This hyperinflammation can damage not only the lungs but also systemic organs, contributing to multi-organ failure in severe cases of COVID-19 (X. Li et al., 2024; Huang et al., 2020).

SARS-CoV2 also reduces the availability of ACE2 on the cell surface, limiting its ability to perform its normal protective functions. Indeed, ACE2 is involved in the renin-angiotensin system (RAS) in which it cleaves angiotensin II (Ang II) into angiotensin 1-7 (Ang1-7) (X. Li et al., 2024). The balance of the Ang II and Ang 1-7 controls the homeostasis of the cardiovascular and renal systems and regulates extracellular fluid volume (Patel et al., 2016). Ang II binds the G protein-coupled receptor MasR inhibiting the p38 MAPK and nuclear factor kappa B (NF-κB) signaling pathways, exerting expanded tubulars, anti-inflammatory, and anti-fibrotic effects. SARS-CoV2 binding to ACE2 prevent the activation of this system promoting vasoconstriction, pro-inflammatory and pro-fibrosis effects (X. Li et al., 2024).

5
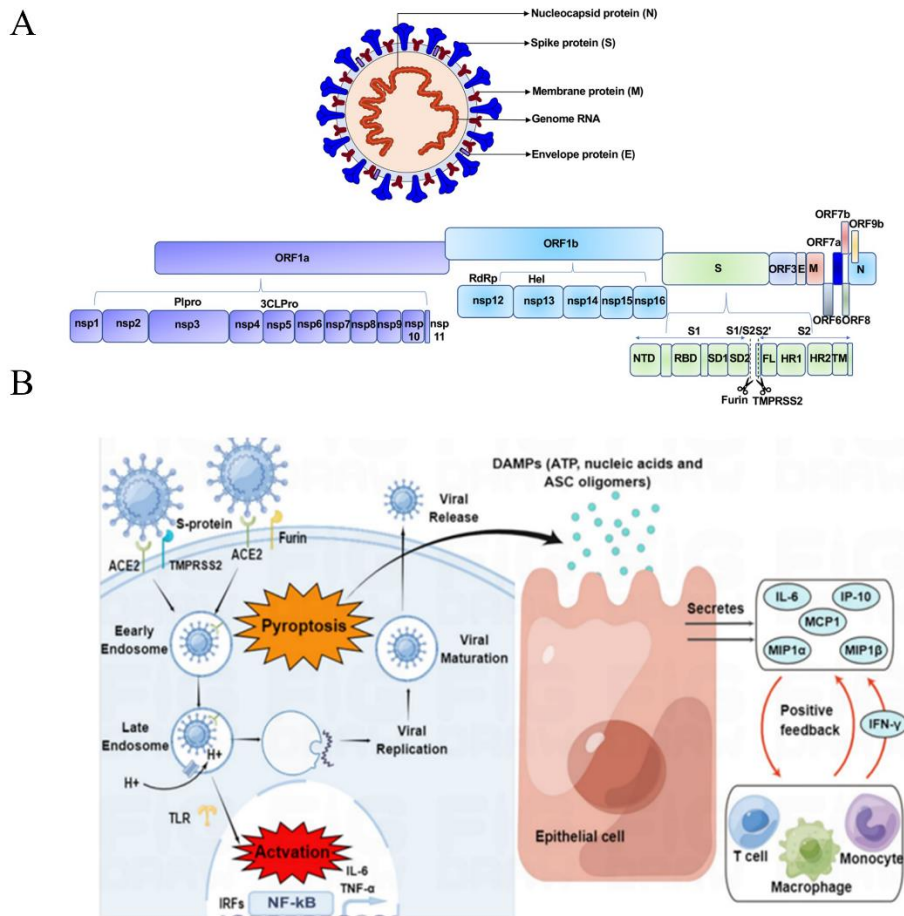
Figure 1: SARS-CoV2 cell entry and effects. (A) Schematic diagrams of the SARS-CoV-2 virus particle and genome. Four structural proteins of SARS-CoV-2 include Spike protein (S), Membrane protein (M), Nucleocaspid protein (N), and Envelope protein (E). The genome including ORF1a-ORF1b-S-ORF3-E-M-ORF6-ORF7 (7a and 7b)-ORF8-ORF9b-N in order is also shown. (B) SARS-CoV-2 entry pathways and immune activation (figure adapted from X. Li et al., 2024 and (Zhang et al., 2021).

2. Spike protein structure and function

The Spike protein (S) is a transmembrane protein with a molecular weight of about 540 kDa. It exists as a homotrimer and each monomer has two functional subunits, called S1 and S2 (Walls et al., 2020b). In the trimer structure, the S1 caps the S2 as shown in figure 2B.

The S1 contains the receptor-binding domain (RBD), which binds ACE2. The other two domains of S1 are the N-terminal domain (NTD) and the subdomains 1 and 2 (SD1/SD2). They play a role in stabilizing the S1 subunit and regulating conformational changes of RBD. Indeed, RBD can assume two conformational states, called "down" and "up", and only the latter exhibits the receptor-binding motif (RBM) that binds ACE2 (M. Y. Wang et al., 2020; Zhu et al., 2021)

The S2 is involved in membrane fusion process required for viral entry into host cells. It is the C-terminal portion of the S protein and it is more conserved among coronaviruses compared to the S1 subunit. It contains several important regions necessary for the fusion of the viral membrane with the host cell membrane that are; fusion peptide (FP), heptad repeat 1 (HR1) and heptad repeat 2 (HR2), central helix (CH), connector domain (CD), transmembrane domain (TM) and cytoplasmic tail (CT) (M. Y. Wang et al., 2020).
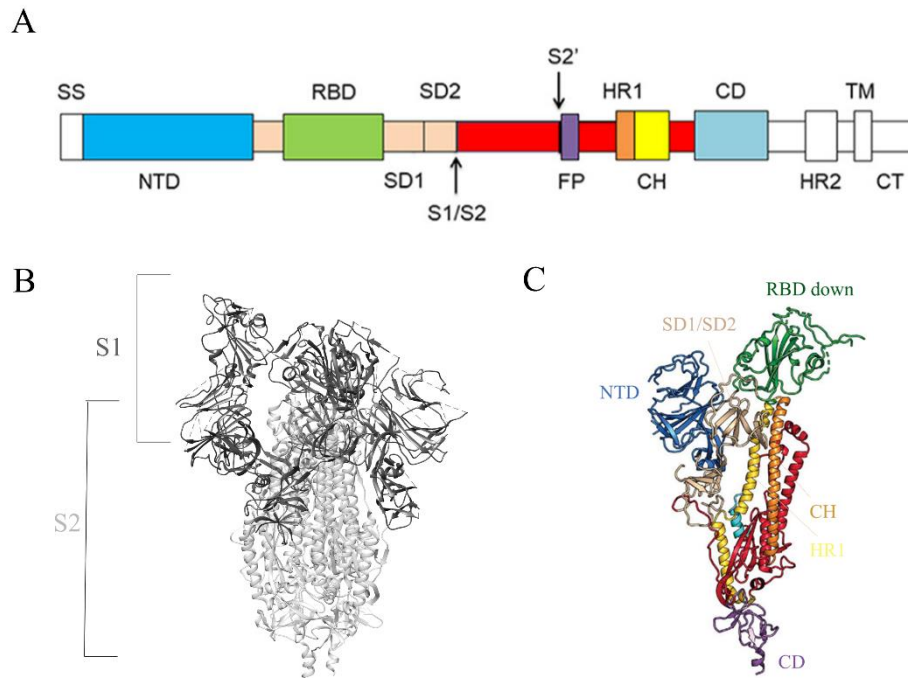
Figure 2: Schematic of SARS-CoV-2 spike structure. (A) Primary structure; SS, single sequence; NTD, N-terminal domain; RBD, receptor-binding domain; SD1, subdomain 1; SD2, subdomain 2; S1/S2, S1/S2 protease cleavage site; S2', S2' protease cleavage site; FP, fusion peptide; HR1, heptad repeat 1; CH, central helix; CD, connector domain; HR2, heptad repeat 2; TM, transmembrane domain; CT, cytoplasmic tail. The protease cleavage site is indicated by arrows (M. Y. Wang et al., 2020). (B) Overall structure of Spike trimer (Image created with UCSF Chimera.). (C) S protein protomer with RBD down that shows the S1 and S2 domains (M. Y. Wang et al., 2020).

2.1 S1 subunit

Starting from the N-terminal region of the S1 subunit, the first domain is the N-terminal domain (NTD), which adopts a structure resembling a β-barrel. This structure is composed of fifteen β-strands that are typically organized into two β-sheets packed against each other in an antiparallel fashion. These β-sheets are connected by loop regions, which play an essential role in interacting with host cell receptors and are also important targets for neutralizing antibodies.

Notably, the NTD of SARS-CoV-2 shares structural similarities with the NTD of SARS-CoV, and comparison studies reveal that this domain is highly conserved between the two viruses (Hussein et al., 2024). This conserved nature of the NTD highlights its importance in the structure and function of the S protein and underscores its potential as a target for therapeutic interventions, including vaccines and neutralizing antibodies. (Du et al., 2021; Klinakis et al., 2021).

The NTD is separated from RBD by a flexible linker region. The linker sequence (RVQPTESIVRFPNIT) contains flexible and unstructured amino acids that allow RBD conformational changes required for interaction with ACE2 (Liu et al., 2023).

The RBD has a core region and a receptor-binding motif (RBM) which directly interacts with the ACE2 receptor. The core of the RBD consists of a five-stranded antiparallel β -sheet structure (β1, β2, β3, β4 and β7). The other two β -sheets, β5 and β6, are in the RBM. RBD has also connecting loops and small α helices that enhance the overall stability. This domain has four disulfide bonds, one in the RBM and the others in the core and it has a N-linked

glycosylation site at position 343, where is located an asparagine (Lan et al., 2020a). This post-translational modification has three roles: immune evasion, structural stability and correct protein folding. (Ives et al., 2024).
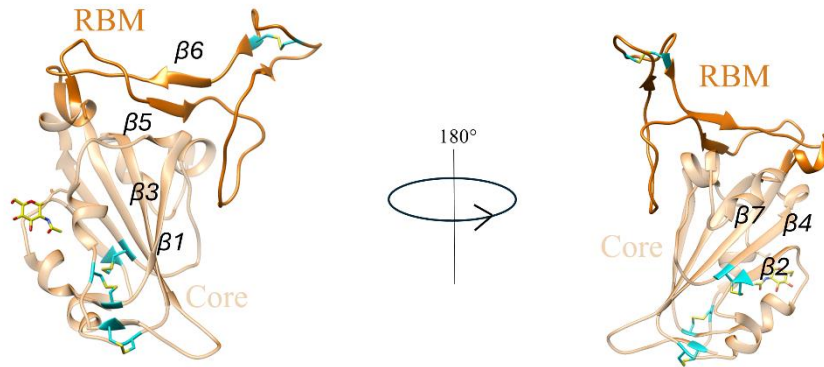
Figure 3: SARS-CoV2 RBD structure (PDB code: 6M0J). This figure shows the residues from 333 to 526. The SARS-CoV-2 RBM is shown in orange and the RBD core is shown in transparency. The four disulfide bonds are shown as sticks and indicated by arrows. The NAG residue is in yellow. Image created with UCSF Chimera.

The receptor-binding domain (RBD) of the spike protein is intricately linked to the S2 subunit through two key domains known as SD1 and SD2. These domains primarily consist of β-strands and α-helices, forming a compact structure that facilitates close interaction with the RBD. SD1 plays a crucial role in stabilizing the RBD in its down position, effectively acting like a "lid" that secures the RBD. This stabilization is achieved through a network of interactions, including hydrogen bonds, van der Waals forces, and electrostatic attractions, all of which work together to maintain the RBD in place. When the

10

RBD transitions to its "up" state, the interactions with SD1 are altered, triggering a conformational change. This transition can be understood from a thermodynamic perspective, as the shift in interactions reflects a change in energy states, facilitating the RBD's movement between these two distinct conformations (Gobeil et al., 2021; Tuvi-Arad & Shalit, 2023; Zekri et al., 2023)

The boundary between the S1 and S2 subunits is a site for proteolytic cleavage, which is necessary for viral entry into the host cell. This site is characterized by a unique polybasic sequence (RRAR). The cleavage is performed by host proteases like furin, and it primes the spike protein for subsequent steps in the fusion process. It separates the S1 subunit, which remains attached to the receptor (ACE2), from the S2 subunit, which undergoes significant conformational changes necessary for fusion with the host cell membrane. This cleavage primes the S protein for subsequent activation by other proteases at the S2' site, which is necessary for the membrane fusion that allows viral entry into the host cell (Davidson et al., 2020; Papa et al., 2021).

2.1.1 RBD conformation changes

In the "down" conformation, the RBD is tucked closer to the rest of the spike protein, hiding the RBM and preventing it from interacting with ACE2. It also allows the virus to escape the immune system, preventing RBM from being recognized by antibodies. By contrast, the RBD in the up conformation interacts with its partner, starting virus entry into the host cells (Wrapp et al., 2020).

The RBD undergoes dynamic fluctuations between these two states, allowing the virus to balance between hiding from the immune system and being ready to bind to ACE2 when it encounters a host cell.

The down state is the lower energy state. In fact, the free energy is minimized due to the intramolecular interaction between the down RBD and the neighbouring domains of the other monomers of the spike protein, such as the NTD of S1 and the HR1 and CH domains of S2. In the "up" conformation, the loss of some stabilizing interactions makes it less stable and represents a higher energy state in the landscape. When the RBD in the "up" conformation binds ACE2, this state becomes energetically favorable thanks to contacts established between the two proteins that lower the overall energy of the complex (Jackson et al., 2022; Le et al., 2023; Walls et al., 2016).

The structural determinants of the interactions between RBD-ACE2 were clarified by solving high-resolution structure of the complex using x-ray crystallography (Lan et al., 2020a).

2.1.2 RBD-ACE2 interface

As SARS-CoV RBD, SARS-CoV2 RBD binds the N-terminal peptidase domain (PD) of ACE2, that is a catalytic site primarily involved in enzyme activity. Indeed, ACE2 plays a crucial role in the balance within the renin-angiotensin system (RAS) (Yan et al., 2020; Hussein et al., 2024). The RBD-ACE2 interaction primarily occurs on the surface of the peptidase domain but does not directly involve the zinc-dependent catalytic site of ACE2 (Kuba et al., 2021). More in details, the N-terminal peptidase domain of ACE2 has two

lobes, forming the peptide substrate binding site between them. The RBM of
RBD contacts the bottom side of the small lobe of ACE2, with a concave outer
surface in the RBM that accommodates the N-terminal helix of the ACE2 (Lan
et al., 2020b).
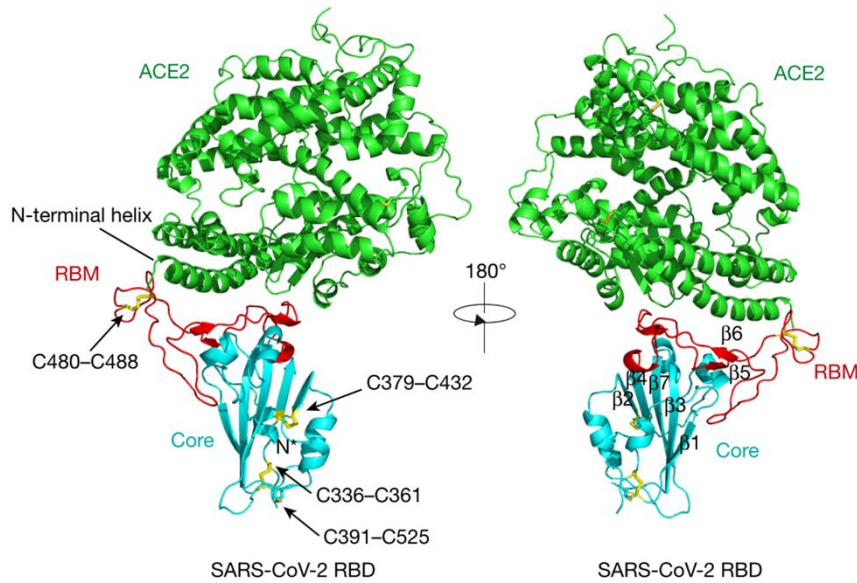
Figure 4: Overall structure of the SARS-CoV-2 RBD bound to ACE2. ACE2 is shown in green. The
SARS-CoV-2 RBD core is shown in cyan and RBM in red. Disulfide bonds in the SARS-CoV-2 RBD
are shown as sticksand indicated by arrows. The N-terminal helix of ACE2 responsible for binding is
labelled (Lan et al., 2020b).

The interaction between the receptor-binding domain (RBD) of SARS-CoV-2
and ACE2 can be categorized into three main types of contacts:

- Hydrogen Bonds: Specific residues in ACE2, such as Y41, Q42, K353, and R357 from the α1 and α3 helices, form a network of hydrogen bonds with residues Q498, T500, and N501 of the RBD. This network is crucial for stabilizing the binding between the two proteins

- Electrostatic Interactions: Additionally, residues D30 and H34 of ACE2 engage in electrostatic interactions with L417 and Y453 of the RBD, respectively. These interactions enhance the affinity and specificity of the binding

- Van der Waals Forces: The interaction is further reinforced by Van der Waals forces, particularly where F486 of the RBD interacts with M82 of ACE2. This type of interaction contributes to the overall stability of the complex (Lan et al., 2020b; Yan et al., 2020)
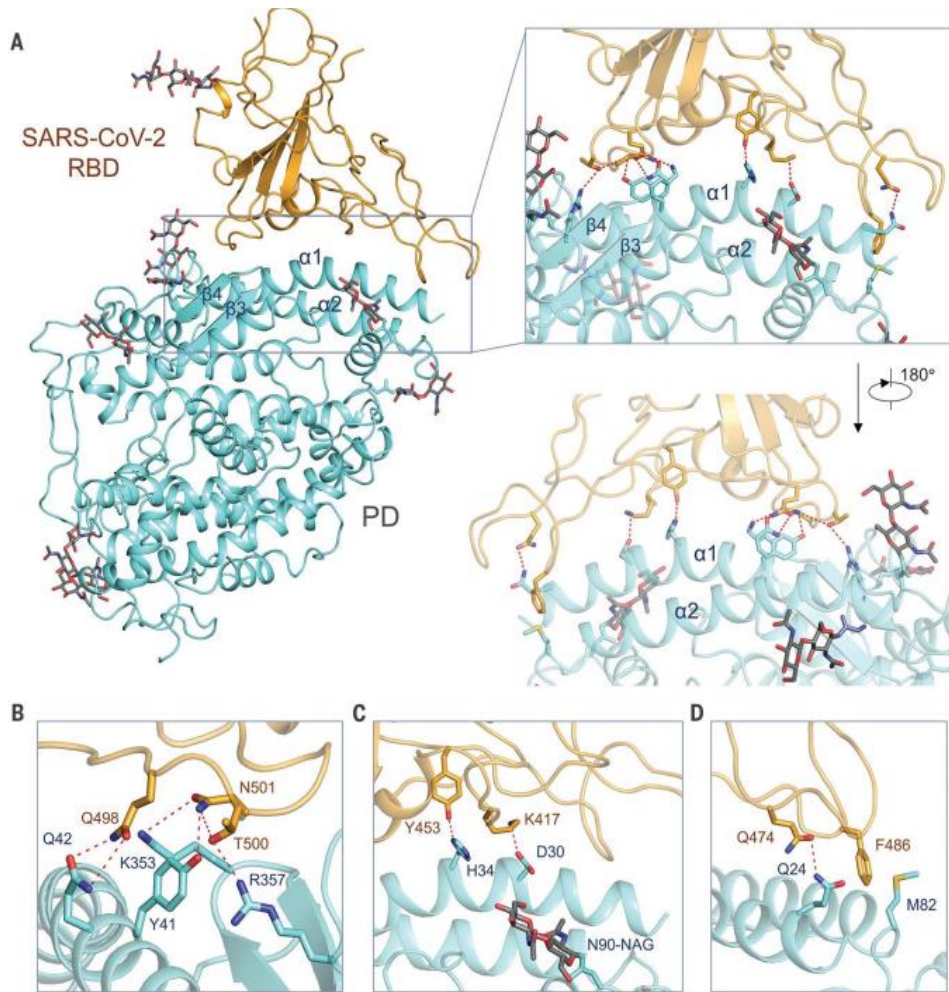
Figure 5: Interactions between SARS-CoV-2- RBD and ACE2. (A) The PD of ACE2 mainly engages the α1 helix in the recognition of the RBD. The α2 helix and the linker between β3 and β4 also contribute to the interaction are shown. (from B to D) Detailed analysis of the interface between SARS-CoV-2-RBD and ACE2. Polar interactions are indicated by red dashed lines (Yan et al., 2020).

2.2 S2 subunit and membrane fusion

After the SD1/SD2 cleavage, a further cleavage at the S2' site by host cell proteases, such as Transmembrane protease serine 2 (TMPRSS2) or cathepsins triggers the final structural rearrangements of the spike protein. The first protease is on the surface of host cells, particularly in the respiratory tract. By contrast the cathepsins are found in the acidic environment of the endosomes. Indeed, they are cysteine proteases, particularly cathepsin L and B, that promote endosomal entry, an alternative route of virus entry. Both proteases cleave the S2' cleavage site, located immediately upstream of the fusion peptide (FP). The precise cleavage typically happens after the R residue at position 685 in the SARS-CoV-2 S protein sequence (Papa et al., 2021).

The S2 subunit of S protein consists of several key domains that are crucial for the virus's entry into host cells and subsequent fusion with the host membrane. Ordered from the end of the S1 subunit, the key domains of the S2 subunit are fusion peptide (FP), Heptad Repeats (HR1 and HR2), Transmembrane Domain and C-terminal Domain (CT), as shown in figure 2A.

This cleavage facilitates the transition from a pre-fusion to a post-fusion state, which is necessary for the fusion process to occur effectively. In the pre-fusion state, the S1 and S2 domains are closely associated and S protein is an metastable state, energetically unfavourable conformation that is not yet fully activated for membrane fusion. More in details, S1 protects the prefusion conformation of S2 in which HR1 bends back toward the viral membrane and it is not close to HR2, preventing the conformational variation required to assume the post fusion conformation. Indeed, both HR1 and HR2 regions are

buried within the Spike trimer through interactions with CH regions and other domains of S2 (Cai et al., 2020). After the cleavage at S1/S2 by host proteases, the dissociation of S1 allows the exposure and extension of the HR1 and HR2 regions allowing the FP to recognize the host cell membranes. Indeed, the FP of S2 is a short, hydrophobic segment that embeds itself into the host cell membrane. This state of S2 subunit is called "fusion intermediate". Subsequent structural rearrangement of HR1 and HR2 leads to the formation of six-Helix Bundle (6-HB), which allows the viral membrane to fuse with the host membrane and subsequent fusion and allows the spike protein to reach the post-fusion state (Dodero-Rojas et al., 2021a; Miner et al., 2022). The bundle consists of three HR1 helices and three HR2 helices in which the first ones form a coiled-coil structure while others wrap around the central HR1 helices, creating a bundle of six helices in total. The HR1-HR2 interaction creates a hydrophobic core that is essential for the stability of the 6-HB, overcoming the energy barrier for membrane fusion (Dodero-Rojas et al., 2021; Papa et al., 2021).
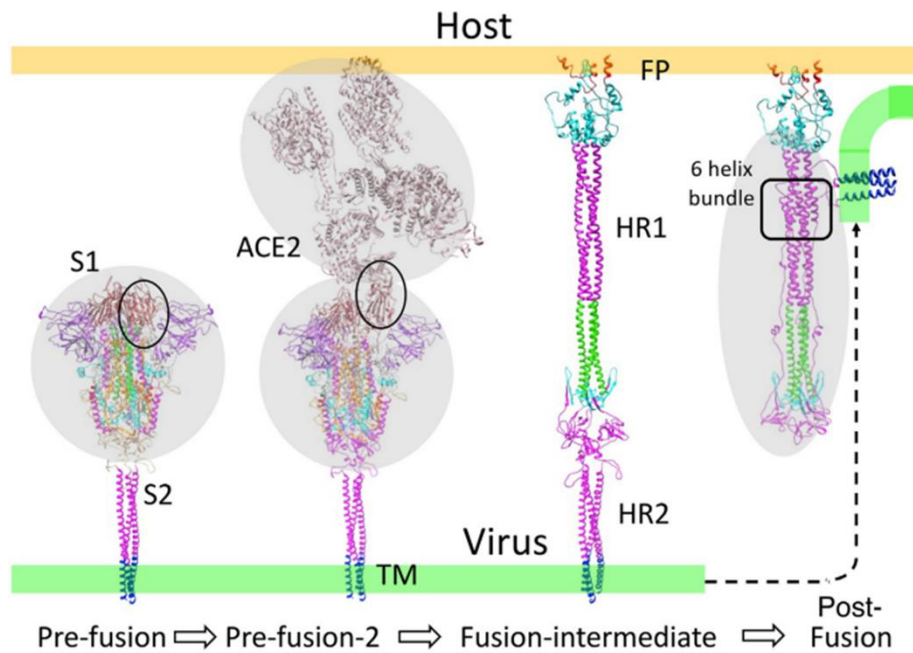
Figure 7: Four different states of the S protein along the pre-fusion to post-fusion transition pathway. Grey shaded regions are known protein structures from the PDB; unshaded regions are not. Transition 1 (from the pre-fusion to the pre-fusion-2 state) involves the receptor-binding domain (RBD) going from a "down" to an "up" conformation (black ovals) in order to bind the host cell receptor ACE2 (B0AT1). Transition 2 (from the pre-fusion-2 state to the fusion-intermediate state) involves formation a long triple-helix with most of the S protein, as well as two heptad repeat domains (HR1 and HR2 in magenta). In this 'fusion-intermediate' state, the fusion peptide region (FP) of the S protein can insert into the host cell membrane. Transition 3 (from the fusion-intermediate state to the post-fusion state) involves the 6-helix bundle (black box) between the HR2 domain and the HR1 domain, which brings the viral membrane into proximity with the host cell membrane and allows the initiation of membrane fusion (Miner et al., 2022).

18

The structural rearrangement of S2 allows the outer leaflets of the viral and host membranes to merge first in a process known as hemifusion. Then inner leaflets merge, creating a fusion pore, a small opening through which the viral genome can enter the host cell (Miner et al., 2022). In the absence of TMPRSS2, the virus may be internalized via endocytosis. Inside endosomes, the acidic environment and other proteases like cathepsins can facilitate S activation and subsequent fusion within the endosome, leading to the release of viral RNA into the cytoplasm (Petersen et al., 2020)

3. SARS-CoV-2 variants

SARS-CoV-2 has undergone many mutations over the years that have allowed it to evade immune responses and potentially become more transmissible. These mutations have led to the development of various variants of concern (VOCs) (Markov et al., 2023)

3.1 Alpha, Beta, Gamma and Delta variants

The mutations of VOCs are summarized in the following figure.
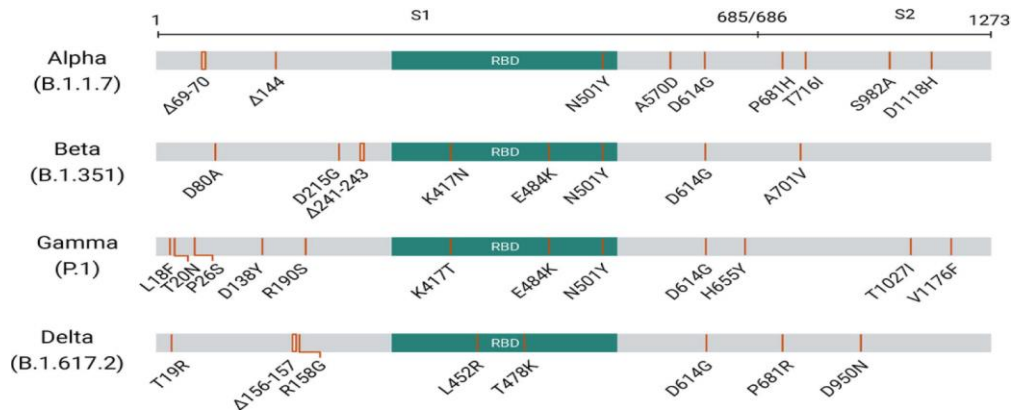
Figure 8: SARS-CoV2 variants. The spike mutations of five worrisome variants are depicted in this graphic (VOCs). (Manjunath et al., 2022)

Some mutations located in the RBD region enhance the affinity of this domain for ACE2 and so they increase transmissibility. This is the case with the first mutation identified, N501Y, which is found in the Alpha, Beta and Gamma variants. The substitution of asparagine in tyrosine at position 501 introduces a new hydrogen bond with Y41 of ACE2, enhancing the interaction between the S protein and ACE2. This stronger binding facilitates entry of the virus into host cells, leading to increased infectivity (Cheng et al., 2021). The E484K mutation, found in the Beta and Gamma variants of SARS-CoV-2, enhances the electrostatic complementarity between the receptor-binding domain (RBD) and ACE2. This mutation facilitates a more stable binding interaction, which can contribute to increased infectivity (Dejnirattisai et al., 2021). Clinical studies have shown that this mutation plays a significant role in immune evasion, as antibodies generated against earlier strains of the virus often exhibit reduced efficacy against variants harbouring the E484K mutation (Harvey et al., 2021; Uwamino et al., 2022). Other mutations, such as K417N identified

20

in the Beta variant or K417T in the Gamma variant, have a critical role in the immune evasion rather than increasing binding affinity. Indeed, the Beta and Gamma RBD showed a lower affinity for ACE2 (H. Bai et al., 2024; Pondé, 2022). It is due to the lack of salt bridge formation between L417 and D30 of ACE2, which determines a decrease oinoverall affinity (H. Bai et al., 2024; Yan et al., 2020).
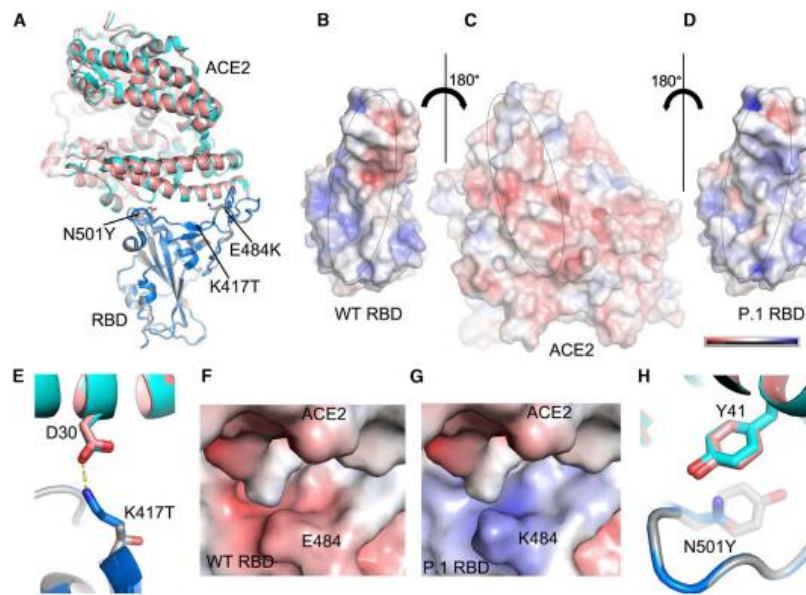
Figure 9 Effect of VOCs mutation. (A) Comparison of Gamma RBD-ACE2 (gray and salmon) with WT RBD-ACE2 (blue and cyan) (PDB: 6LZG) by overlapping the RBDs. The mutations in the Gamma RBD are shown as sticks. (B–D) Open-book view of electrostatic surface of the WT RBD-ACE2 complex (B) and the Gamma RBD/ACE2 complex (C and D). Note the charge difference between the WT and the mutant RBDs. (E) The K417 of the WT RBD forms a salt bridge with D30 of ACE2 (Dejnirattisai et al., 2021).

The L452R mutation enhances the RBD affinity for ACE2 receptor introducing a positively charged amino acids, as arginine, which forms stronger interactions with the negatively charged regions on the ACE2 receptor. In Delta variant, in addition to L452, the substitution of threonine (T) in lysine (K) at position 478 increase the binding affinity for ACE2 thanks to the introduction of a positive charge in that can enhance the electrostatic interactions between the spike protein and the ACE2 receptor. The presence of positively charged residue at 478 position allows the formation of electrostatic interactions or hydrogen bonds with the negatively charged D30 and E35 of ACE2. These mutations prevent also the recognition by antibodies (Y. Wang et al., 2022).

Another significant effect of mutations, particularly in the Beta variant, is the stabilization of the RBD in its down conformation. The E484K and N501Y mutations contribute to this stabilization by disrupting critical salt bridges that would normally support the closed state of the RBD. While this stabilization hinders antibody recognition, the presence of mutations that enhance the RBD's affinity for ACE2 facilitates its transition to the up state when the spike protein approaches the receptor (Valério et al., 2022).

3.2 Omicron variant

Compared to previously described variants, the Omicron variant has many mutations in the S protein, leading to a significant increase in viral

transmission, immune evasion and vaccine efficacy. Since Omicron emergence in late 2021, it has rapidly evolved, leading to the development of several subvariants. The most notable and widespread subvariants are BA.1, BA.2, BA.4 and BA.5 (Q. Wang et al., 2022)
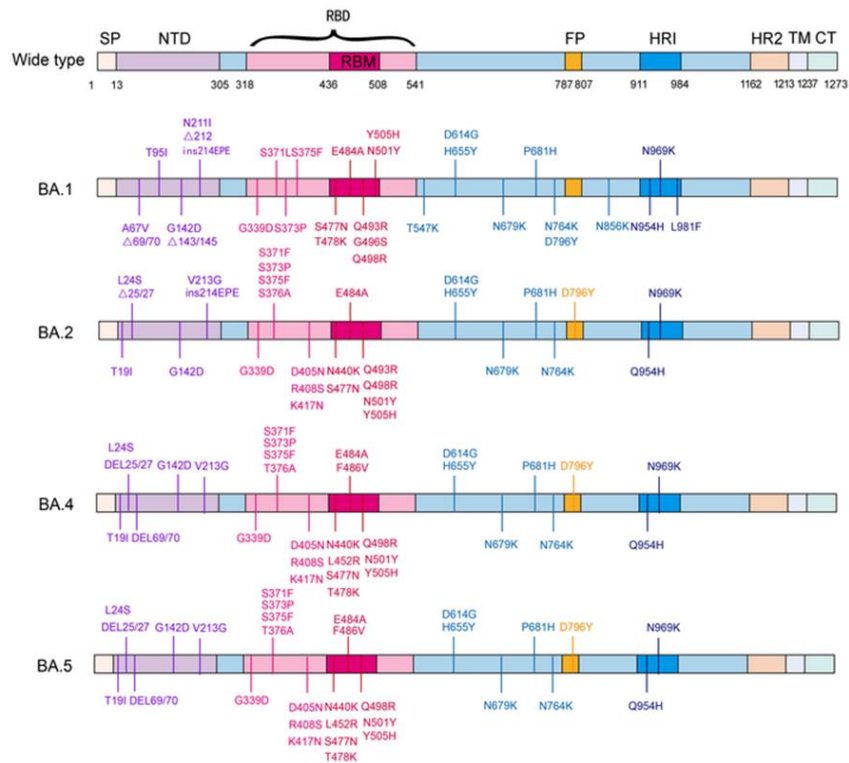
Figure 10. Schematic representation of Omicron subvariants mutations. The RBD and RBM region is shown in shallow violet red and deep violet red respectively, and the N-terminal domain (NTD) region is demonstrated in bluish violet (adapted from Xu et al., 2022).

23

In the Omicron variant, a specific RBD loop containing the mutations S371L, S373P, and S375F facilitates inter-protomer interactions between adjacent "down" RBDs. According to the Cryo-EM structure of the BA.1 S ectodomain (Stalls et al., 2022), the S373P mutation induces rearrangements that enhance the packing of the RBD-RBD interface. This allows the region with S373P and S375F to interact with the regions containing N501Y and Y505H in the neighbouring down RBD. Consequently, this stabilization of the "down" conformation hinders antibody recognition (Gobeil et al., 2022; Stalls et al., 2022).

Compared to the Delta variant, which is the last identified before Omicron, BA.1 has also mutation such as G339D, K417N, N440K, S447N and Q498R that decrease the binding affinity for ACE2 but prevent antibody recognition. Omicron BA.1 and Delta variant have comparable affinity for ACE2. Indeed, the negative effect of these substitutions in Omicron BA.1 is compensated by other crucial mutations that enhance RBD affinity for ACE2, such as N501Y, T478K, Q493R, G496S, and Q498R. The first three mutations are present also in the previously found variants. In Omicron RBD, the mutated residue Y501 makes π-stacking interactions with Y41 in ACE2, as previously seen in the Alpha, Beta, and Gamma variants. By contrast, the other mutations were found for the first time in Omicron RBD and their role in RBD affinity for ACE2 was clarified by Cryo-EM, as shown in figure 11 (Mannar et al., 2022). Arginine at position 498 forms a new salt bridge with ACE2 residue D38 while maintaining a hydrogen bond interaction with ACE2 residue Q42 (Li et al., 2023). Also, serine in position 496 adds a new interaction at the interface by forming a hydrogen bond with ACE2 residue K353 (Mannar et al., 2022; Hossen et al., 2022).
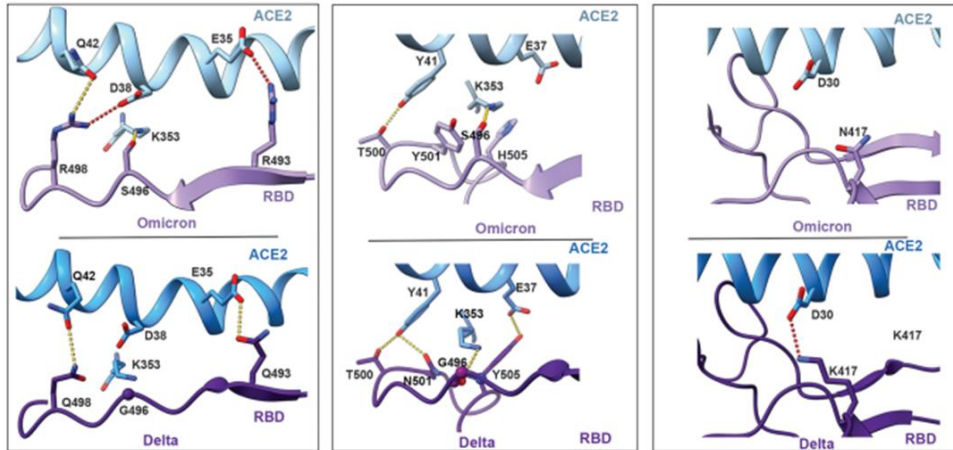
Figure 11: Comparison of the RBD-ACE2 interface between the Omicron (top) and Delta (bottom) variants. Compared with the Delta variant, new interactions are formed as a result of the mutations Q493R, G496S, and Q498R and local structural changes owing to the N501Y and Y505H mutations present in the Omicron variant. The salt bridge between Delta RBD K417 and ACE2 D30 that is present in the Delta variant spike protein but lost in the Omicron variant is highlighted in yellow and red dashed lines represent hydrogen bonds and ionic interactions, respectively (Mannar et al., 2022).

The second widespread Omicron subvariant is called BA.2. It shares the same amino acids sequence with BA.1 with three additional mutation with a crucial role, which are S371F, T376A, D405N, and R408S (de Souza et al., 2023) The BA.2 phenylalanine at position 371 results in van der Waals interaction of the bulkier F371 side chain with F342, promoting the closer packing of the two helical stretches 339–342 and 367–371 within the RBD. The interprotomer packing of these two helical stretches leading to a more compact RBD fold may be responsible for the increased thermostability observed for the BA.2 RBD relative to the BA.1 RBD. The mutation T376A located in a β strand

disrupts the hydrogen bond between the hydroxyl group of threonine with the main chain of A435 in the adjacent β strand. In this way, this mutation pulls along the region around the S375F substitution so that F375 can now reach over to stack against the G404-Q409 helix and the V503 side chain of the adjacent protomer. In the restructuring of the 371–376 loop, concerted changes also occur in the adjacent protomer RBD that are key for forming the new interactions. The BA.2 R408S substitution results in the disruption of an interprotomer hydrogen bond that the residue R408 side chain makes with the main chain carbonyl of residue 375. This releases F375 and facilitates its movement toward the adjacent RBD. The loss of the interprotomer H-bond due to the R408S substitution may be compensated by the BA.2 D405N substitution that mediates an interprotomer H-bond with the main chain carbonyl of Y369. The differences induced by additional mutations are shown in figure 12 (Stalls et al., 2022).
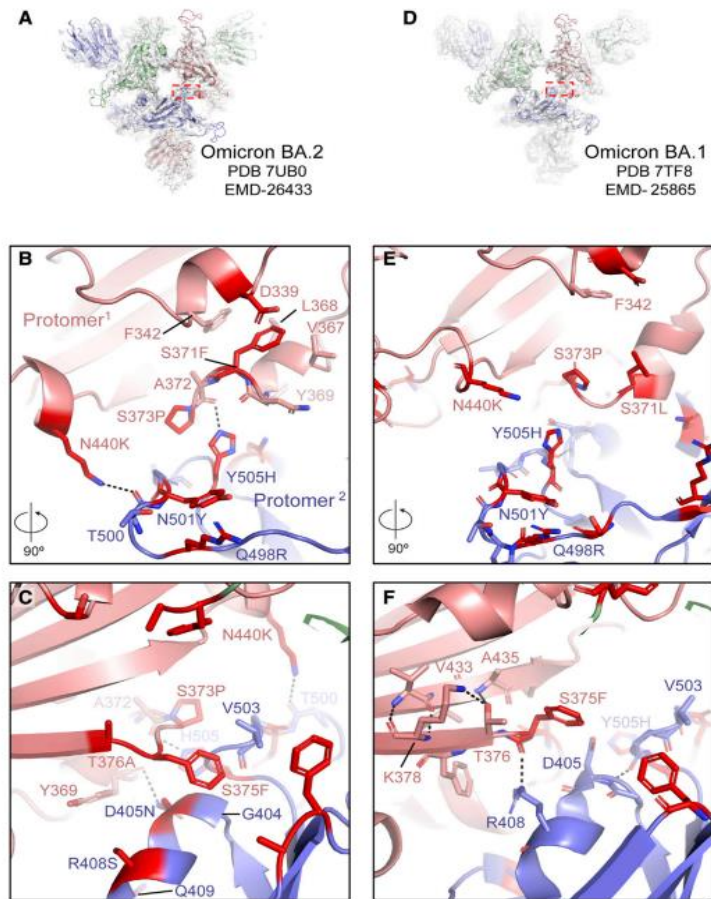
Figure 12: Omicron BA.2 mutations induce RBD interfacial loop remodeling, facilitating tight packing of the 3-RBD-down state. (A) View of the Omicron BA.2 S protein O1 BA.2 state with the red dotted rectangle indicating the region shown in (B) and (C). (B and C) 90 rotated views of the interface between two RBDs in the 3-RBD-down O1 BA.2 structure. The sites of mutation are colored red and the residues shown in sticks. (D) Same as (A) but for the Omicron BA.1 S protein O1 state (O1 BA.1), with the red rectangle indicating the region shown in (E) and (F). (E and F) Same as (B) and (C) but for the Omicron BA.1 S protein O1 BA.1 structure (Stalls et al., 2022)

27

The latest variants, BA.4 and BA.5 have identical S proteins, most like BA.2. Relative to BA.2, BA.4 and BA.5 have the additional RBD mutations, L452R, F486V and wild-type amino acid at position Q493. As in the Delta variant, L452R mutation increases RBD affinity for ACE2. In wild-type RBD phenylalanine at position 486 interacts with ACE2 and mutations of this residue have been associated with a reduction in neutralizing activity of antibodies. The lack of mutation at 493 position restores the contacts identified between wild-type RBD and ACE2 (Tegally et al., 2022).

4. Monoclonal antibodies against RBD

The inherent ability of the virus to mutate has made it difficult to identify an effective therapy based on neutralizing antibodies (NAbs). So far, most of the NAbs identified recognize RBD but as described above, many mutations of SARS-CoV2 variants in this domain prevent recognition by NAbs, sometimes even at the expense of affinity for ACE2.

Based on the epitope recognition and binding mode, RBD-specific NAbs are categorized into 4 major classes (I, II, III, and IV). The first two classes, I and II, recognize the RBM, preventing the interaction with ACE2 and then the virus entry into host cells. For this reason, these Nabs are also called "ACE2 blockers". The class I can bind RBD only in the up state. By contrast NAbs belonging to the second class bind RBD in both states, "up" and "down".

Class III NAbs are like class II NAbs and can recognize adjacent RBD protomers. The last class contains NAbs that bind the conserved region of RBD present in the core structure (Kumar et al., 2021).

The identification of NAbs against SARS-CoV2 is complicated due to the high mutation rate of the virus. An effective therapy can exploit two strategies: the use of NAbs that bind a conserved region of the antigen or the combination of Nabs that binds different epitopes (Kumar et al., 2021) The fist strategy is the one used by S309, which is part of Sotrovimab, a monoclonal antibody therapeutic that has been authorized for emergency use in treating COVID-19 patients. One of the key binding interactions of S309 involves the glycan residue at N343 of the RBD and the surrounding protein residues that are not involved in the interaction with ACE2 (McCallum et al., 2022). The second strategy is the case of a therapeutic antibody cocktail developed by Regeneron, REGN-CoV2. It comprises Casirivimab and Imdevimab which target distinct, non-overlapping epitopes on the RBD**.** By binding to different parts of the spike protein, the cocktail provides strong neutralizing activity against the virus and helps prevent viral escape due to mutations (Focosi et al., 2024).

Aims of the work

The impact of SARS-CoV-2 has been profound on multiple fronts, affecting public health, economies, and social structures globally. As the virus spread in early 2020, it caused the COVID-19 pandemic, leading to millions of infections and deaths worldwide. The therapeutical strategies against SARS-CoV-2 involve mainly vaccine and monoclonal antibodies. Many neutralizing monoclonal antibodies (NAbs) that specifically recognize RBD of SARS-CoV-2 S protein have been identified in convalescent patients. The continues identification of SARS-CoV-2 variants in the recent years jeopardizes the design of effective broadly NAbs. Common therapeutical strategies involve the use of NAbs that recognize conserved epitopes or the use of NAbs cocktails simultaneously binding multiple regions of the antigen.

In 2020, with the aim to develop a broadly NAbs, Takis S.r.l. company produced a large library of antibodies that recognize RBD of S protein using hybridoma technology (D'Acunto et al., 2024). The immunization was carried out on Balb/c mice with a plasmid vector encoding the full-length S protein and the recombinant RBD-hFc protein. The Th2-dominant immune response performed by Balb/c mice allows the production of a wide variety of antibodies. Following this, a large library of murine antibodies (more than 2000) was produced and the murine antibodies which showed a high affinity for the human RBD were selected and subjected to the chimerization process. It consisted in cloning the identified murine variable regions into expression

vectors, encoding the human IgG1 heavy chain constant and the human light chain kappa constant domains. A promising combination of chimeric antibodies, involving the chimeric 9-8F2-B11 and 3-12B12-F4, was identified (D'Acunto et al., 2024) and it has been demonstrated that it can neutralize all SARS-CoV2 variants (D'Acunto et al., 2024). Starting from the chimeric 9-8F2-B11 complementary determining regions (CDRs), which are the regions of Abs responsible for antigen recognition, the corresponding humanized antibody was generated. The humanization process consists of the substitution of murine framework regions with common human amino acidic sequences. This is critical for antibodies produced using hybridoma technology for therapeutic purposes, as it allows the immunogenicity to be reduced.

The primary aim of this work is to functionally and structurally characterize the humanized antibody, 9-8F2-B11. Functional and binding experiments were mainly performed in the Takis research laboratories allowing us to determine the K_D and the ND50 of this antibody for wild-type S protein and the VOCs. Single particle cryo-electron microscopy (cryo-EM) technique was used for structural studies on wild-type S protein bound to 9-8F2-B11 Fab, allowing the identification of the recognized epitope, which is crucial for further antibody engineering to make it effective against the newly emerging SARS-CoV2 variants.

Beyond its primary therapeutic application, the ability to compare the binding properties and activity of both chimeric and humanized antibodies against different strains of SARS-CoV-2 presents a significant scientific opportunity. This comparison not only deepens our understanding of these antibodies' efficacy across viral variants but also sheds light on the effect of antibody

humanization process on their activity. By studying how humanization influences binding affinity and neutralizing activity would be possible to optimize the design of more effective therapeutic antibodies.

To further investigate these aspects, the affinity and activity of the humanized antibody characterized in this work were compared to the previously reported values for the chimeric 9-8F2-B11 antibody. To identify the structural factors responsible for the observed differences in affinity and activity, a preliminary Cryo-EM data collection and image processing were performed on the complex formed between the chimeric 9-8F2-B11 Fab fragment and the S protein. This result will enable a deeper exploration of the molecular determinants driving these changes, contributing to advancements in antibody engineering and therapeutic development.

Materials and methods

1.   Cell Culture

Expi293 and Expi293 GnTI$^-$ cells were maintained in Expi293 cell medium (Thermo Fisher Scientific) between $0.3x10^6$ and $3x10^6$ cells per mL. ExpiCHO cells were maintained in ExpiCHO Expression Medium (Thermo Fisher Scientific) between $0.3x10^6$ and $6x10^6$ cells per mL. The HEK293TN-hACE2 cell line was generated by lentiviral transduction of HEK293TN cells. The HEK293TN cells were obtained from System Bioscience, Palo Alto, CA, USA.

2. Cloning, expression, purification

2.1 Receptor Binding domain (RBD)

The gene of the extracellular domain of the wild type RBD and its variants with a C-terminal 6xHis-tag was cloned into a plasmid property of Takis S.r.l., optimized for the expression in Expi293 and Expi293-GnTI$^-$ cell lines. The latter cell line does not have N-acetylglucosaminyltransferase I (GnTI) activity

and therefore lacks complex N-glycans. The construct was transfected with ExpiFectamine 293 (Thermo Fisher Scientific) into 400 mL of Expi293 suspension cells cultured to $3x10^6$ cells per mL at 37 °C, 5% CO_2 following a standard expression protocol indicated by the producer. Briefly, the DNA:ExpiFectamine complex was incubated in Opti-MEM™ I Reduced Serum Medium (Thermo Fisher Scientific) for 20 minutes before adding it to the cell culture. ExpiFectamine 293 Transfection Kit enhancers 1 and 2 were added 18-22 hours post-transfection, and penicillin-streptomycin (pen/strep) after 6-8 hours more. The supernatant was collected 7 days after the addition of the enhancers and was at first collected in 50 mL tubes (Falcon) and then centrifuged at 12,000 rpm for 30 minutes to eliminate most of the cellular debris. Once the cells were removed, supernatant was filtered with 0.2 μm filters (Stericup Millipore Merck) for the following step of purification. Briefly, the supernatant was diluted with a 1:1 ratio with the equilibration buffer (50 mM NaH_2PO_4, 300 mM NaCl, 5 mM Imidazole pH 8.0) and loaded at a flow rate of 1 mL/min overnight at 4°C onto a PureCube 100 Compact Cartridge Ni-NTA (Cube Biotech), pre-equilibrated with the same equilibration buffer mentioned above, using the ÄKTA pure protein purification system (Cytiva). After loading, the column was washed with a solution of 50 mM NaH_2PO_4, 300 mM NaCl pH 8.0 and the protein was eluted with the Elution buffer (50 mM NaH_2PO_4, 300 mM NaCl, 300 mM Imidazole pH 8.0). These steps were carried out at a flow rate of 1 mL/min. For a transfection of 400 mL of suspension cells, the obtained yield was about 10 mg. Finally, the protein was dialyzed using the Slide-A-Lyzer (Thermo Fisher Scientific) overnight at 4 °C in PBS 1X.

2.2 Spike ectodomain

Expi293 cells were transfected using the SARS-CoV-2 S HexaPro (Plasmid #154754) (Hsieh et al., 2020) The gene of Spike ectodomain has mutations in the S2 subunit, which stabilises the Spike protein and enhances expression. In detail, amino acids in the furin site (682-685) are replaced by 'GSAS' and other mutations (F817P, A892P, A899P, A942P, K986P, V987P) are present. The transfection was carried out into 200 mL of Expi293 following the same protocol of RBD. The supernatant was collected 4 days after the addition of the enhancers and first collected in 50 mL tubes (Falcon) and then most of the cellular debris was removed by centrifugation at 12,000 rpm for 30 minutes. The supernatant was diluted with a 1:1 ratio with the equilibration buffer (10 mM Tris, 500 mM NaCl, 20 mM Imidazole pH 8.0) and protein purification was carried out using Ni-NTA resin slurry (Cube Biotech) with overnight incubation at room temperature. Then resin has been washed with the wash buffer, which is the same of the equilibration buffer. Purified spike ectodomain was obtained by elution with 10 mM Tris, 500 mM NaCl, 30 mM Imidazole pH 8.0. At the end, size exclusion chromatography (SEC) was performed as further purification step. 500 μl of sample was injected and the run was carried out at a flow rate of 0.75 mL/min in 20mM Hepes pH 7.5 and 200mM NaCl using Superdex 200 Increase 10/300 GL column.

2.3 Antibodies

The genes of the recombinant light and heavy chains of the antibodies were cloned into a plasmid, both property of Takis S.r.l., optimized for the expression in ExpiCHO cell line. The constructs were transfected with ExpiFectamine CHO (Life technologies) into 400 mL of ExpiCHO suspension cells cultured to $6x10^6$ cells per mL at 37 °C, 5% CO_2 following a standard expression protocol indicated by the producer, using Opti-MEM™ I Reduced Serum Medium (Invitrogen). ExpiFectamine CHO Transfection Kit enhancers 1 and 2 were added 18-22 hours post-transfection, and pen/strep after 6-8 hours more. Cells were collected with the same method described above for the Expi293 cells. For the purifications, the supernatant was diluted with a 1:1 ratio with the equilibration buffer (100 mM NaH_2PO_4/Na_2HPO_4 pH 8.0) and loaded at a flow rate of 1 mL/min overnight at 4°C onto a ToyoScreen AF-rProtein A HC-650F column (Tosoh bioscience), pre-equilibrated with the same equilibration buffer mentioned above, through the ÄKTA pure protein purification system (Cytiva). In this case, the wash buffer had the same composition as the equilibration buffer, instead for the elution was used 100 mM citrate buffer pH 3.0. These steps were conducted at a flow rate of 1 mL/min. For a transfection of 400 mL of suspension cells, the obtained yield was about 20 mg for both antibodies. In the end, chimeric and humanized 9-8F2-B11 were dialyzed overnight at 4 °C in PBS1X.

3. Biolayer Interferometry

Binding studies were carried out using the Octet Red system ForteBio. All steps were performed at 25 °C, with shaking at 600 rpm in a 96-well plate containing 200 µL of solution in each well. A kinetics buffer 1X (ForteBio) was used throughout this study for the antibody and analyte dilution and for washing the sensors. Kinetics assays were performed by first capturing the humanized antibody using anti-human Fc Octet biosensors. The biosensors were soaked for 10 min in 1X kinetics buffer, followed by baseline signal measurement for 60 s and then loaded with humanized Ab (10 µg/mL) for 300 s (until the biosensor was fully saturated). After a wash step in 1X kinetics buffer for 120 s, the mAb-captured biosensor tips were then submerged for 300 s in wells containing different concentrations of the antigen (RBD-6xHis) to evaluate the association curves, followed by 900 s of dissociation time in the kinetics buffer. The binding curve data were collected and then analyzed using data analysis software v11.1 (ForteBio). Binding sensorgrams were first aligned at the beginning of the antigen binding cycle and following the single reference subtraction. The K_D values were calculated using a 1:1 global Langmuir binding model. The humanized Ab captured biosensor tips were also dipped in wells containing the kinetics buffer to allow single reference subtraction to compensate for the natural dissociations of the captured mAb.

37

4. Pseudovirus neutralization assay

To obtain a neutralization assay with lentiviral particles, HEK293TN-hACE2 cells were plated at 10,000 cells/well in white 96-well plates in complete DMEM medium. After 24 h, the cells were transduced with 0.1 MOI of SARS-CoV-2 pseudovirus, previously incubated with a serial 3-fold dilution of antibody, in order to obtain a 7-point dose– response curve. Briefly, 5 µL of each antibody dilution was added to 45 µL of DMEM medium containing the pseudovirus and incubated for 1 h at 37 ◦C. Then, 50 µL of the antibody/pseudovirus mixture was added to each well and the plates were incubated for 24 h at 37 ◦C. Each point was assayed in triplicate. After 24 h of incubation, cell transduction was measured by the luciferase assay using the Bright-Glo™ Luciferase Assay System (Promega) and an Infinite F200 plate reader (Tecan). The measured relative light units (RLUs) were normalized with respect to the controls and the dose–response curves were generated and the neutralization dose 50 (ND50) was calculated with GraphPad Prism using a non-linear regression curve fitting.

5. RBD deglycosylation

The RBD 6xHis tagged, expressed in Expi293-GnTI$^-$, was fully deglycosylated using EndoH$_f$ enzyme (New England Biolabs). The protein was first dialyzed in a buffer containing 20 mM Tris pH 8.0 and 150 mM NaCl. It was then

incubated overnight with EndoH$_f$ enzyme, adding glycobuffer (0.5 M Sodium Acetate pH 6.0) for a final dilution of 1:10. The following day, the sample was retrieved and RBD was purified from the EndoH$_f$ enzyme using pre-equilibrated PureCube 100 Ni-NTA agarose resin (Cube biotech) during an overnight incubation at 4 °C. The equilibration buffer used was 50 mM NaH$_2$PO$_4$, 300 mM NaCl, and 5 mM Imidazole at pH 8.0. Finally, the sample was centrifuged at 1,300 rpm and the supernatant containing the EndoH$_f$ enzyme was discarded. The resin underwent washing with a pH 8.0 buffer containing 50 mM NaH$_2$PO$_4$ and 300 mM NaCl, and the fully deglycosylated protein was eluted using a buffer containing 50 mM NaH$_2$PO$_4$, 300 mM NaCl, and 300 mM Imidazole pH 8.0. The eluted fractions were assessed by SDS-PAGE and glycostaining, utilizing the Pierce™ Glycoprotein Staining Kit (Thermo Fisher Scientific), and then pooled together.

6. Fab fragments generation

The chimeric and humanized antibodies was digested using Papain enzyme. Subsequently, the antibodies were dialyzed in 20 mM NaH$_2$PO$_4$/Na$_2$HPO$_4$, 5 mM EDTA pH 7.0 and incubated overnight at 37°C with papain-conjugated resin (Thermo Fisher scientific). Prior to incubation, the resin was equilibrated with 20 mM NaH$_2$PO$_4$/Na$_2$HPO$_4$, 5 mM EDTA, 20 mM L-Cysteine•HCl pH 7.0. Finally, the sample was recovered and centrifuged to discard the resin. The mixture of Fc and Fab fragments and undigested antibodies were incubated overnight with ToyoScreen AF-rProtein A HC-650F resin (Tosoh bioscience), equilibrated before with a buffer containing 20 mM NaH$_2$PO$_4$/Na$_2$HPO$_4$ pH 7.0. The day after, the sample was centrifuged and the supernatant, containing

the Fab fragments, was collected. The undigested antibodies and Fc fragments were eluted with 100 mM Citrate buffer pH 3.0.

7. RBD-Fab crystallization trials

For crystallization trials, the deglycosylated RBD and the Fab of humanized 9-8F2-B11 antibody were mixed in a 1:1.5 stoichiometric ratio, with a stoichiometric excess of Fab and incubated for 1 hour at 4°C. The sample was then injected into a Superdex 200 increase 10/300GL column for size-exclusion chromatography, in order to isolate the RBD-Fab complex. The column was previously equilibrated with a buffer containing 150 mM NaCl and 10 mM Tris-HCl pH 8.0. The experiment was conducted using a flow rate of 0.5 mL/min. The complex was concentrated at 7.5 mg/ml and 10 mg/mL and was subjected to automated crystallization trials by means of an Oryx4 crystallization robot (Douglas Instruments). We tested various conditions using commercial screens, including INDEX (Hampton Research), Morpheus and Proplex (Molecular Dimension), JCSG++ and PACT++ (Jena Bioscience). Upon inspecting the plates under the microscope, we identified a promising crystallization condition containing 0.1M Hepes pH 7.0 and 15% PEG2000. We manually optimized this using the hanging drop method, adjusting the pH (7.0 to 8.0) and PEG concentration (8% to 25%). The initial condition was replicated on crystallography plates using "cat's whisker" method seeding. The crystals obtained were sent to the ELETTRA synchrotron (Trieste, Italy) but diffracted at low resolution (~10 Å), insufficient for determining atomic positions. To enhance crystal growth quality, we also employed random Microseed Matrix Screening (rMMS) using the Oryx4 crystallization robot.

8. Spike-Fab single particle cryo electron microscopy (Cryo-EM)

8.1 Negative staining

The most conventional and fast procedure to assess sample quality, homogeneity prior the cryo-EM experiment is to visualize it by negative staining EM (NS-EM) at room temperature. This experiment is very quick, easy to perform and inexpensive. For a NS experiment, few microliters of the sample are applied on a grid and coated with a stain containing heavy atoms (e.g., uranyl acetate), and subsequently dried. This procedure allows to image biological specimen since the electron-dense stain increases the contrast (the signal-to-noise ratio) of the image and data collection does not need to be carried out at low temperature.

For the NS-EM of the S protein, the purified sample (concentrated 2 mg/ml) was diluted 1:30 in SEC buffer (20 mM Hepes, pH 7.5, and 150 mM NaCl). After glow discharge, 5 µL of diluted sample was applied to carbon-coated copper grids. After ~1 minute, the excess liquid is blotted away, and a drop of uranyl acetate was applied. The stain is allowed to interact with the sample briefly for 1 minute and then blotted off. The grid was examined using the standard 120 kV electron microscope JEOL JEM1400 available at the Cryo EM facility of the CNB-CSIC. The quality and homogeneity of the sample were optimal and therefore we decided to use it to prepare Cryo EM grids.

8.2 Sample preparation

For the Cryo EM experiment, purified S protein was mixed with the humanized Fab in a 1:3.5 stoichiometric ratio, ensuring an excess of Fab. Various conditions were tested to optimize complex formation, including different temperatures and incubation times. Specifically, the Spike- humanized 9-8F2-B11 Fab complex was prepared at 37°C with overnight and two-hour incubation periods.

Sample preparation for cryo-EM requires the application of the specimen to be imaged on a grid, reducing the solution to a thin layer. We used Quantifoil® gold grids coated with a layer of carbon. These grids are used in Cryo EM because the gold base reduce the beam-induced motion and has better heat and electrical conductivity, which prevents image distortion and damage to the sample. The regular distribution of the holes over the grid later facilitates the procedure of automatic data collection. Since the support surface is highly hydrophobic, grids are usually treated and hydrophilized with low-energy plasma (glow discharger), to allow a homogeneous spreading of aqueous solutions and retaining particles on the grid surface.

According to the approach developed by Jacques Dubochet and colleagues (Dubochet et al., 1985)., the general procedure of grid preparation and vitrification, called plunge freezing, were carried out. Nowadays this procedure provides for the use of a robotic semi-automatic cryo-plunger cryo-plunger containing a chamber with controlled temperature and humidity. We used the Vitrobot Mark IV (Thermo Fischer Scientific) operating at 4 °C and 100% humidity. A droplet of 3 μL of the Spike-Fab complex was applied on a

grid previously glow-discharged for 1 minute at 40 mA using a GloQube system (Quorum Technologies). After its application on the grid, the sample is incubated for a certain time (waiting time) and the excess liquid is wicked away blotting the grid with filter paper before plunging it in liquid ethane cooled at liquid nitrogen temperature for vitrification. For the screening we tested different vitrification conditions, varying the blotting force (2 and 3) and the sample concentration (1.2 mg/ml and 0.6mg/ml). Each grid was prepared in duplicate. The blotting force refers to the pressure applied during the blotting step that affects how much liquid is retained on the grid, which in turn influences the thickness of the ice film. Sample concentration is a critical parameter that must be carefully optimized. If the concentration is too high, it can lead to particle overlap on the grid, making it difficult to resolve individual particles. Conversely, if the concentration is too low, there may be insufficient particle density, leading to inadequate data collection for reliable structure determination.

Vitrification was carried out by rapidly plunging the grid into liquid ethane cooled at liquid nitrogen temperature, around -180 °C. Plunge-frozen grids were tested on a FEI Talos Arctica (Thermo Fischer Scientific) 200 kV microscope at the cryo-EM facility of the CNB-CSIC (Madrid, Spain), initially collecting a low number of images to evaluate sample quality, particle concentration and distribution in the grid holes and the ice thickness, prior a more extensive data collection. The initial screening of the prepared grids allowed the selection of the best two grids, that contains the most adequate number of well separated particles, that were then used for data collection. The grids selected were prepared by incubating the sample with concentration of 1.2 mg/ml and with blot force 2. The grids differ in the incubation time used

to form the complex. In the first grid the complex was incubated overnight and in the second grid it was incubated for two hours.

Cryo EM grids of the chimeric 9-8F2-B11 Fab in complex with S protein were also vitrified, according to the best vitrification conditions identified for the humanized Fab.

8.3 Data collection

Cryo-EM data of the humanized Fab – S protein complex were obtained with overnight data acquisition at the Cryo-EM facility of CNB-CSIC using a FEI Talos Artica (Thermo Fischer Scientific), a 200k field emission electron microscope equipped with Falcon 4i direct electron detector. The specimen was constantly maintained at cryogenic temperature. Using the last EPU software version, we did a multi grid data collection that allow us to collect data across multiple grids in a single session without manual intervention between grids.

Image acquisition was carried out with a nominal magnification of 120,000×, corresponding to a calibrated pixel size of 0.85 Å on the object scale, at nominal defocus values ranging between -0.8 and -2.2 μm. 3372 movies were recorded and used for the data processing.

The data collection of the chimeric Fab was also carried out at the Cryo-EM facility of CNB-CSIC. Approximately 1900 movies were collected and processed.

8.4 Cryo EM image processing

8.4.1 Humanized 9-8F2-B11 – S protein

Collected data of humanized 9-8F2-B11 Fab – S protein was imported in Scipion 3.0 for all the subsequent analysis steps. Movie frames were aligned and dose-weighted using MotionCor2 to correct beam-induced overall movement across the image (Zheng et al., 2017). Contrast transfer function (CTF) was estimated with CTFFIND4.1 (Rohou and Grigorieff, 2015) on aligned and non-dose-weighted micrographs. Micrographs showing evident ice contamination were removed and those reporting resolution estimate of 5 Å or better were selected for further analysis. For the particle picking, xmipp tool was used. In the first step, to generate particle templates, more than 100 particles were manually picked from several micrographs with different defocus values. Using the manually picked particles as reference, the automatic particle picking was performed, resulting in 116,870,4 picked particles, with a subsequent extraction using a particle box size of 450 pixels, rescaled to 200 pixels to speed up the calculations.

Two rounds of 2D classification were carried out. In this process, particles are rotated, translated in all possible orientations, and matched to each other, then averaged together to form a certain number of classes containing different views of the specimen. Particles not representing any view are removed at this step, cleaning up the dataset. A total of 155,796 particles selected from several 2D classes was used to generate six ab initio 3D models reconstructed from the different orientations of the particles. The decision to use six 3D classes for

45

model reconstruction was made to thoroughly investigate the conformational heterogeneity present in the sample.

The most detailed and populated map of the six generated was selected for subsequent first refinement cycle, performed using C3 symmetry. After in the second cycle of refinement the symmetry was release by setting the symmetry to C1, which represents no symmetry. In this way the symmetry constraints during refinement to accurately model asymmetric regions.

These first refinements were carried out using non-uniform refinement tool of CryoSparc and 3D autorefine of Relion, both available in Scipion 3.0.

A local refinement was then performed to improve the quality of the map using one mask that includes the three RBD-Fab fragments interfaces.

3D flex correction tool of Cryosparc was used to address the conformational flexibility in macromolecular complexes. Indeed, when particles exhibit significant flexibility, averaging all conformations together results in blurry regions because different parts of the structure are in different positions in different particle images. 3D flex correction separates or corrects for different states of the molecule, allowing for clearer visualization of each state.

	Humanized 9-8F2-B11 – S protein
Magnificatiom	120,000×
Voltage	200
Electron exposure (e-/Å2)	47
Defocus range (µm)	-0.8 and -2.2
Pixel size (Å)	0.85
Symmetry imposed	C3
Initial particle images	~1,000,000
Final particles images	104,126
Map resolution	3.6

Table 1. Data collection and image processing parameter of humanized 9-8F2-B11 in complex with S protein summary.

To further improve the resolution of the RBD down-Fab and RBD up-Fab interfaces, the map obtained from local refinement was used to generate two separate maps: one focused on the RBD down-Fab interface using a mask specific to that region, and another map focused on the RBD up-Fab interface with a different mask applied to isolate that area. The output masked maps were use for the post-processing sharpening.

The local resolution of these map was determined using the Local Resolution tool implemented xmipp3, available in Scipion. It allowed us to investigate how resolution is distributed throughout the density map for both the RBD down-Fab and RBD up-Fab interfaces. For these maps the resolution at the interfaces is between 4 and 4.5 Å. It is crucial to do an accurate model building.

47

8.4.2 Chimeric 9-8F2-B11 – S protein

The chimeric 9-8F2-B11 Fab – S protein data processing was carried out using CryoSparc. The 1912 micrographs were imported in CryoSparc, aligned and dose-weighted using Motion correction tool. A blob picker was performed to identify and select particle-like features (blobs) from micrographs. A first 2D classification was then carried out to select the best 2D classes that were used for the template picking. 811,000 particles were extracted using 450 as box size rescaled to 200.

The extracted particles were used for five cycles of 2D classification in which 2D classes having particles that do not correspond to the sample under investigation were removed. After the last 2D classification only 9,501 particles were obtained and used for the Ab initio model. This model was then refined using non-uniform refinement. The global resolution was around 5.5 Å. The data collection and processing parameters are summarized in Table 1.

	Chimeric 9-8F2-B11 – S protein
Magnificatiom	120,000×
Voltage	200
Electron exposure (e-/Å2)	39
Defocus range (μm)	-1.0 and -5.0
Pixel size (Å)	0.84
Symmetry imposed	C3
Initial particle images	~800,000
Final particles images	9,501
Map resolution	5.5

Table 2. Cryo EM data collection and processing parameters chimeric 9-8F2-B11 in complex with S protein summary.

8.4.3 Model building and single particle analysis

Following the density of maps reconstructed by single particle analysis, the initial atomic model for S protein in complex with humanized 9-8F2-B11 Fab was assembled as follows. Coordinates of the previously deposited structure of S protein (7FB1) and the predicted alpha fold model of humanized 9-8F2-B11 Fab were used as a starting model to build the atomic model.

The map of the S protein - humanized Fab complex chosen for model building was the one reconstructed imposing a C3 symmetry, releasing symmetry, and local refined showing a global resolution of 3.7 Å. The initial atomic models were initially rigid body positioned in the final local refined map using USCF Chimera, followed by real space refinement tool available in Phenix, model building and refinement procedure manually performed using Coot.

In the same way the model building of RBD down -Fab and RBD up – Fab complexes were carried out using the map obtained by masking the interfaces. Only the RBD of S protein was used as initial model. Indeed, unlike the previous map, there was not enough resolution in the rest of the map to make an accurate fit. The model was refined using tool in Phenix and the model building and manual refinement in still ongoing.

Results and discussion

1. The humanized 9-8F2-B11 binds the RBD of the S protein with high affinity

We measured the dissociation constant (K_D) using a biolayer interferometry (BLI) assay. The humanized antibody was immobilized on the surface of an anti-human Fc biosensor tip. The biosensor was then dipped into a solution containing the RBD of the S protein, allowing interaction with the immobilized antibody. The BLI system detects changes in the interference pattern of light reflected from two layers: the sensor surface and an internal reference. As the analyte (RBD) binds to the antibody bound to the sensor, the increase in molecular mass at the sensor surface alters the interference pattern.

The system monitors the binding of the analyte to the sensor over time (association phase) and the rate at which it dissociates when moved into a buffer solution without analyte (dissociation phase). This real-time kinetic data enables the calculation of the association rate constant (k_a) and the dissociation rate constant (k_d), from which the affinity constant (K_D) is derived as the ratio between k_a and k_d.

The assay was performed with serial dilutions of the wild-type RBD (ranging from 150 nM to 2.34 nM). Experiments were conducted similarly with the most widespread RBD variants; Alpha, Beta, Gamma, Delta, along with BA.1 and BA.4/5 Omicron.
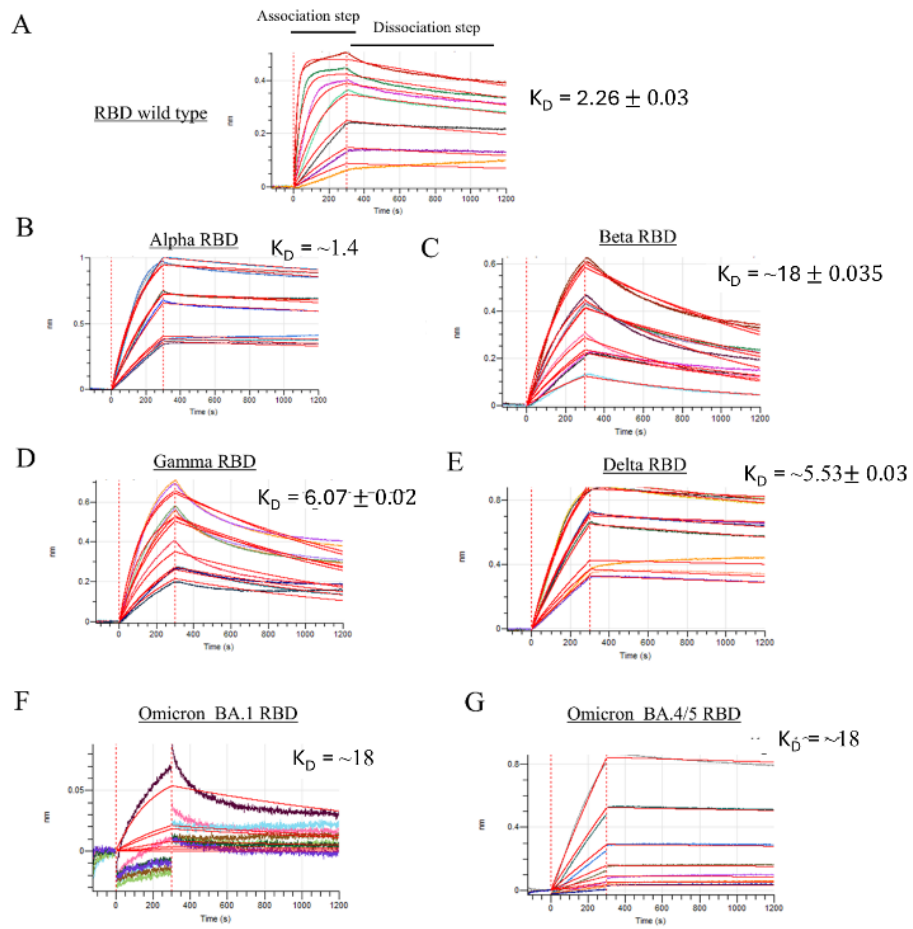
Figure 13: Sensorgrams obtained through BLI assays. The sensorgrams at different concentrations with the relative fit (red lines) are shown in Figures **A, B, C, D, E, F** for wild type RBD and for alpha, beta, gamma, delta, BA.1 and BA4/5 RBD strains, respectively. The corresponding determined K_D value is reported for each RBD.

51

Comparison of the affinity of the humanized antibody with that of the corresponding chimeric antibody, reported in the Table 3 showed that the humanization process did not affect the affinity for all RBD variants, except for the Omicron BA.1 subvariant. Indeed, the affinity reported for the chimeric antibody is about 3.7 nM (D'Acunto et al., 2024), while the one determined for the humanized antibody is about 18 nM. The almost five times lower K_D indicates that the variations in the amino acid sequences of the Fab framework regions affect the antibody affinity for the Omicron BA.1 subvariant. By contrast, a significant increase of affinity is observed for the Beta variant.

	Wild type	Alpha	Beta	Gamma	Delta	BA1	BA4/5	Reference
Chimeric 9-8F2-B11	1.9	1.21	73	3.9	2.39	3.7	18	D'Acunto et al. 2024
Humanized 9-8F2-B11	2.26 ± 0.03	~1.4	18 ± 0.035	6.07 ± 0.02	5.53± 0.03	~18	~18	This work

Table3: Comparison of the K_D values between the chimeric and the humanized 9-8F2-B11. All the K_D value are in nM.

2. Neutralizing activity of humanized 9-8F2-11 against the entire S protein

To investigate the ability of humanized antibody to prevent virus entry into the host cells, we performed a pseudovirus neutralization assay using HEK293TN-hACE2 cells and a pseudovirus carrying the S protein on its surface, which lacks the full set of genes required to initiate an infection. The pseudovirus contains a gene report, that in this case is the gene that encode for luciferase.

When it enters the host cells, luciferase is expressed and, in the presence of oxygen and ATP, it converts the substrate luciferin in oxyluciferin, together with light, carbon dioxide (CO_2), and water (H_2O). The light emitted is measured with a luminometer and is directly proportional to the entry of the virus into the host cells.

The addition of NAbs that prevents RBD binding to ACE2 determines a reduced pseudovirus entry into the host cells and with the consequent reduction of the expression of luciferin, inducing a decrease in emitted light measured.

We performed this assay using antibody concentration with a serial 3-fold dilution, in order to obtain a 7-point dose–response curve. The measured relative light units (RLUs) were normalized with respect to the controls and the dose–response curves were generated and the neutralization dose 50 (ND50) was calculated using a non-linear regression curve fitting. Here we defined the ND50 as the antibody concentration required to reduce infected cells by 50%. Low values indicate an efficient inhibition RBD binding to ACE2, that occurs even at low concentrations.

Using pseudovirus with alpha, beta, gamma and delta S protein variants we determined also the ND50 of humanized 9-8F2-B11 against SARS-CoV2 variants.
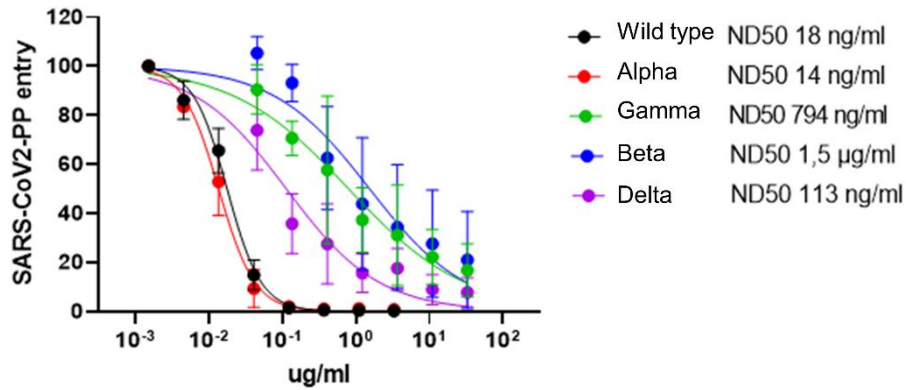
Figure 14. Neutralization curve obtained from the pseudovirus neutralization assay. The obtained ND50s are reported.

The lower values calculated using wild-type, alpha and delta variants indicate that humanized 9-8F2-B11 is more efficient against these variants than against beta and gamma variants.

This assay was performed also with pseudovirus that has Omicron BA.1 and BA4/5. In the former case, we did not observe a reduction of the emitted light. This indicates that the humanized antibody is not able to prevent the BA.1 binding to ACE2. In the case of BA.5, we conduced a preliminary assay (data not shown) in which we observe no significant differences if compared to the chimeric antibody (ND50 o~570 ng/ml (D'Acunto et al., 2024)).

Table 4 reports the ND50 calculated for the humanized 9-8F2-B11 against SARS-CoV2 variants tested in this work compared with the ND50s previously determined for the chimeric antibody (D'Acunto et al., 2024). This higher values of ND50 calculated for the humanized antibody indicate a lower neutralizing activity.

54

This is consistent with other works in which is reported that changes in the Fab framework regions during the humanization process affect the structural conformation and stability of the antibody reducing the its activity (Safarzadeh Kozani et al., 2024;Wu et al., 1999).

	Wild type	Alpha	Beta	Gamma	Delta	BA1	BA4/5	Reference
Chimeric 9-8F2-11	11	8	175	57	127	-	570	D'Acunto et al. 2024
Humanized 9-8F2-B11	18	14	1500	794	113	--	~570	This work

Table4. Comparison of the ND50 values calculated for chimeric and humanized 9-8F2-B11. All values are in ng/ml

3. Crystallization trials

To identify the epitope of the humanized 9-8F2-B11, we initially sought to determine the structure of the RBD – humanized Fab complex using X-ray crystallography. The critical step in the process is protein crystallization, which involves the formation of a highly ordered, solid crystal lattice from a protein solution. Achieving this requires a highly pure and homogeneous protein sample. In addition to the aforementioned factors, the size and structural complexity of the sample can significantly hinder crystallization.

To enhance our chances of successfully obtaining structural information about the interaction between the humanized antibody and the S protein through X-ray crystallography, we specifically expressed and purified only the RBD for the complex formation. Indeed, the previously ELISA assay (D'Acunto et al.,

55

2024) and our BLI assays confirmed that both the chimeric and humanized antibodies effectively bind to this domain (described in the methods section) (Ilari & Savino, 2008; Wlodawer et al., 2013).

3.1 Fab fragment generation

A whole antibody is rarely used in biology x-ray crystallography due to its structural complexity, flexibility and size which make crystallization very challenging. Instead of the whole antibodies, Fab fragments are generally used because they are smaller and more rigid allowing for more successful structural determination.

For this purpose, the recombinantly chimeric and humanized antibodies were expressed and purified from ExpiCHO cells and treated with papain-conjugated resin. Papain acts on specific peptide bonds at the region indicated by the arrow in figure 15; in particular, papain cleaves after an arginine or lysine preceded by a hydrophobic residue and not followed by a valine (Collins & Khalili, 2022) The advantage of using papain is that it can reduce the risk of denaturing the antigen-binding regions of antibodies, allowing the antigenic activity of the generated Fab fragments to be preserved. At the end of the papain cleavage, the Fab and the crystallizable fragment (Fc) were obtained. The Fab fragments are separated from the Fc fragments using Protein A resin, which has high affinity and selectivity for the Fc region. This allows efficient isolation of the Fc fragments, leaving the Fab fragments in the flow-through.
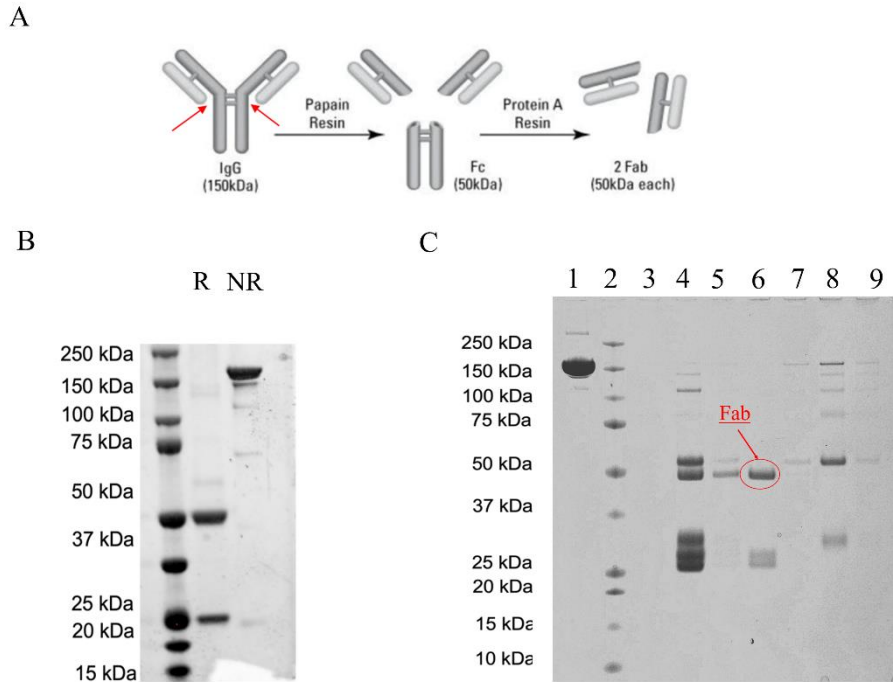
Figure 15: Humanized NAb papain digestion evaluated through SDS-PAGE. **A** Representative scheme of papain cleavage sites from Pierce™ Fab Preparation Kit (Thermo Fisher Scientific). Cleavage sites recognized by papain are indicated by two red arrows. **B** Whole antibody after affinity chromatography with protein A resin used for purification. From left to right: molecular weight standard (MW), antibody sample loaded on SDS page in presence of DTT (R) and antibody in the absence of reducing agent (NR) **C** Digestion and purification of the cleaved Fab. Initial stock of full antibody (1), molecular weight of marker (2), flow-through (3), digestion product (4), digestion wash (5), and washes of the protein A resin (6) containing Fab and elutions containing the Fc fragments and undigested antibody (7, 8, 9).

Starting from ~10 mg of antibody, we managed to obtain a final amount of ~5 mg of Fab. The purified Fab is shown in figure 15C (red arrow).

3.2 RBD purification and deglycosylation

We performed a complete deglycosylation of the RBD which contains two primary N-glycosylation sites located at the following residues: N331 and N343 (Casalino et al., 2020).

At the beginning of this work, we performed crystallization trials using the glycosylated protein, but no crystals were obtained. Indeed, glycosylation often cause sample heterogeneity as due to the possibility of dealing with alternative glycosylation patterns that differently affect protein conformation. This is entirely contrary to the requirement for sample homogeneity in X-ray crystallography. During crystallization, molecules need to arrange themselves into a highly ordered and repeating lattice. If the sample is heterogeneous this disrupts the regular arrangement of molecules. As a result, it becomes significantly more difficult for the crystal lattice to form properly, reducing the possibility to obtain highly diffracting crystals. Glycosylation also introduces flexibility into the protein, which can disrupt crystal packing and lower the resolution of the diffraction data (Nagae & Yamaguchi, 2012).

For this reason, we expressed the RBD-6xHis in Expi293 GnTI⁻ cells, which are engineered to limit protein glycosylation. Indeed, this strain have an inactivating mutation in N-acetyl-glucosaminyltransferase I (GnTI), an enzyme important for adding glucidic residues to proteins during synthesis (Sun et al., 2023). As a result, this cell line lacks complex N-glycans, in contrast to the wild-type Expi293 cells. At each asparagine residue that is normally glycosylated, the glucidic branching is reduced to two N-acetyl glucosamine residues and five mannose residues. The molecular weight of RBD protein expressed in Expi293 GnTI⁻ cells is approximately 30 kDa due to

reduced glycosylation. To obtain a fully deglycosylated protein, endoglycosidase (EndoH$_f$, ~70 kDa) was applied overnight at 4 °C. EndoH$_f$, hydrolyzes the glycosidic bond between the two N-acetylglucosamine (GlcNAc) residues in the core structure of the oligosaccharide attached to the RBD asparagine residue (Huang et al., 2018). In order optimize the yield of deglycosylated protein while minimizing the cost of the process, we initially tested various conditions for the endoglycosidase reaction. Figure 16B shows the SDS-PAGE of the obtained sample of RBD treated and not treated with EndoH$_f$. The reduction in glycosylation can be appreciated by the decrease in the molecular weight of the RBD band.

To remove the endoglycosidase, the sample was loaded onto nickel-conjugated resin. The enzyme elutes in the flow-through, while only the his-tagged RBD elutes with 300mM imidazole (figure 16C).

Through this method, we successfully obtained a pure, fully deglycosylated protein, thus increasing the chances to obtain diffracting crystals.
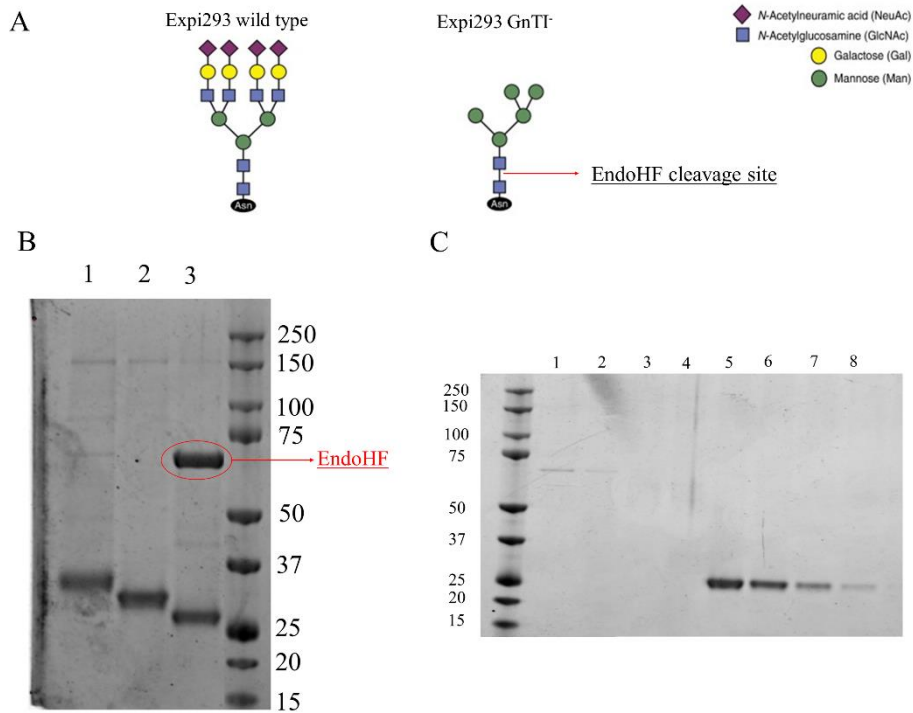
Figure 16: RBD glycosylation. A Representative scheme of glycosylation components and differences between wild type and Expi293 GnTI⁻ cells. The cleavage site of $EndoH_f$ is indicated by one red arrow (adapted from Büssow, 2015). **B** Comparison of RBD molecular weight produced in Expi 293 (1), Expi293 GnTI⁻ (2) and RBD cleaved with $EndoH_f$ (3) on SDS-PAGE. **C** Purification of RBD using nickel-conjugated resin. $EndoH_f$ was present in the flow-through of the resin (1,2,3,4) while RBD eluted with 300mM imidiazole (5,6,7,8).

During the purification and deglycosylation steps of the RBD, we utilized a His-tag to facilitate the separation process. However, the presence of the His-tag can potentially interfere with crystallization. To address this, we decided to remove the His-tag using Tobacco Etch Virus (TEV) protease. The plasmid used to transfect Expi293 GnTI- cells includes a gene sequence positioned between the RBD and the His-tag, which encodes the TEV protease cleavage

60

site. The specific amino acid sequence at this site is ENLYFQG, with cleavage occurring between the glutamine Q and glycine G residues (Enríquez-Flores et al., 2022)

The deglycosylated RBD was incubated overnight at 4°C with His-tagged TEV protease and nickel-conjugated resin. After incubation, the flow-through containing the cleaved RBD was collected. Any uncleaved RBD molecules and His-tagged TEV protease remained bound to the nickel-conjugated resin, allowing an efficient separation them from the His-tag-free RBD.

3.3 RBD-Fab complex crystallization trials

To facilitate complex formation the Fab and RBD were mixed with a stoichiometric ratio 1:1.5, with the RBD in excess. To remove the unbound proteins and obtain a homogeneous sample, the complex was purified using size exclusion chromatography (SEC).
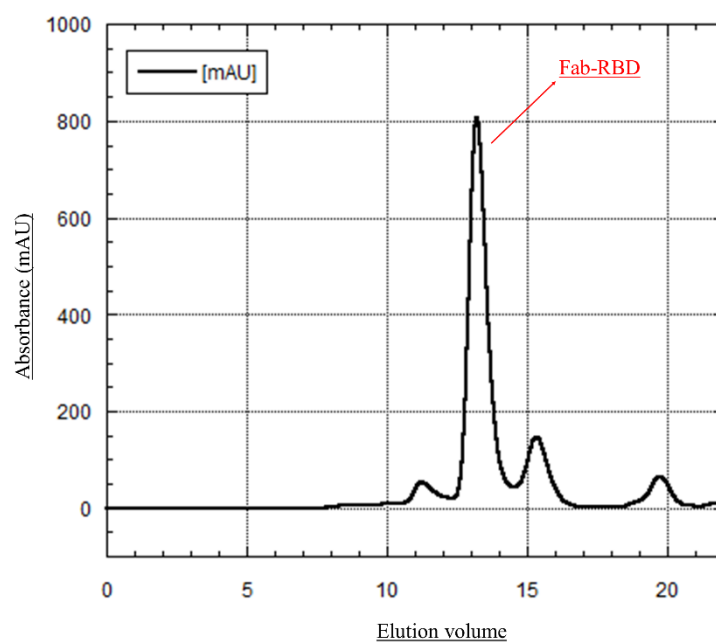
Figure 17: RBD-Fab SEC chromatogram. The peak corresponding to Fab-RBD complex is indicated by red arrow.

We isolated a distinct peak, shown in Figure 18, between 13 and 14 mL of elution volume, corresponding to a molecular weight of approximately 75 kDa. The sample was then concentrated to 7.5 and 10 mg/mL, and subsequently used for crystallization trials.

We performed a high throughput screening of the crystallization trials using the Oryx4 robot. Promising conditions were also optimized by manual setting. Some of the screened conditions enabling formation of crystals, shown in figure 18.

0.1M Hepes pH 7.0 and 15% PEG2000

10% PEG2000 12% PEG2000 15% PEG2000 with seeding
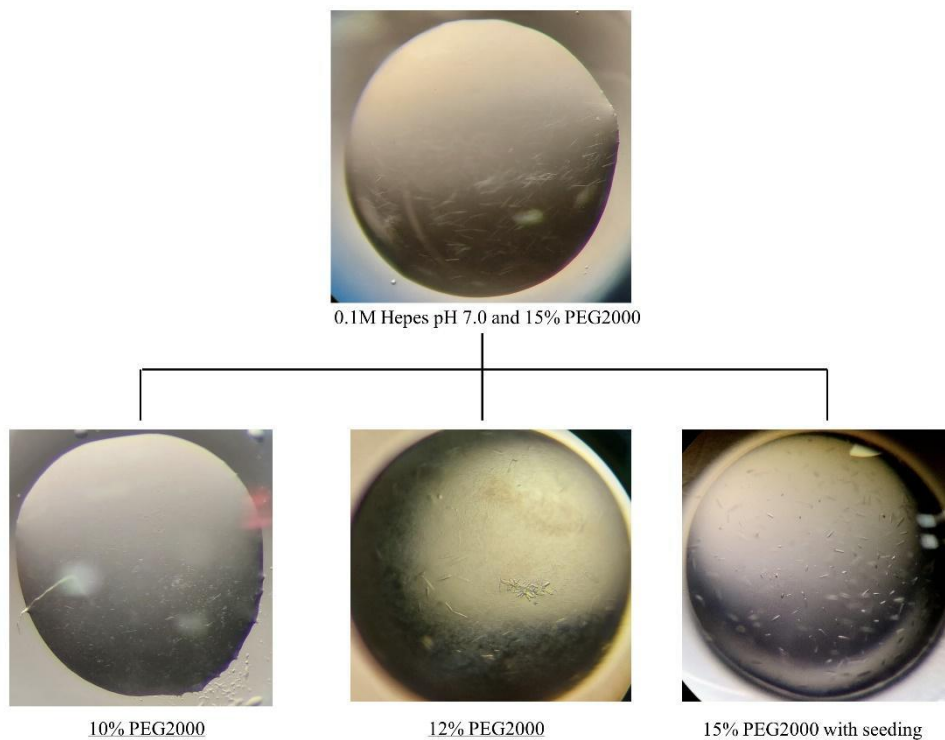
Figure 18: RBD-Fab crystals. At the top, the drop obtained through high-throughput screening is shown, while at the bottom, the best crystallization conditions identified through manual drop optimization are displayed.

The best RBD-humanized Fab crystals, as shown in figure 18, were obtained using the seeding technique. This method involves introducing small crystal fragments (seeds) from previous crystallization experiments into fresh drops, which promotes the growth of larger and better-ordered crystals (Lieu et al., 2020). For this first seeding we used the "cat's whisker" method, in which this thin tool is manually first passed into the drop containing crystals and then into

63

the new drop into which the so-called seeds are to be released (Rutkiewicz-Krotewicz et al., 2018a). Crystals grown with 'cat's whisker' seeding are larger than those grown without this technique. It aligns with the findings of Lieu and colleagues, who highlighted the effectiveness of this approach, particularly for Fab-antigen complexes, where it proves especially useful (Lieu et al., 2020). We tested the diffracting power of the obtained crystals at the ELETTRA synchrotron (Trieste, Italy) but we only observe low resolution diffraction (~10Å).

To improve the quality of crystals, we tried a random Microseed Matrix Screening (rMMS). This technique is fully automated and can be implemented using robotic systems like the Douglas Instruments Oryx4. It offers several advantages: the process is faster, highly reproducible, and significantly less labour-intensive. Most importantly, it enables high-throughput screening, allowing for the efficient placement of seeds into drops with various crystallization conditions, maximizing the likelihood of successful crystal growth (Rutkiewicz-Krotewicz et al., 2018b; Shaw Stewart et al., 2011). Despite using rMMS, the quality of the crystals obtained did not significantly improve compared to those produced by previous methods.

The crystallization attempts yielded no success, prompting us to redirect our efforts toward Cryo-EM. We chose to utilize the advanced instrumentation available at the cryo-EM facility at the Centro Nacional de Biotecnología del Consejo Superior de Investigaciones Científicas (CNB-CSIC) in Madrid, Spain. Indeed, this technique offers significant advantages in the visualization of large and complex biomolecular assemblies, which are often difficult to crystallize.

4. Cryo-EM structure of the humanized 9-8F2-B11 in complex with Spike protein

The primary advantage of Cryo-EM over x-ray crystallography is that it does not need protein crystallization to obtain near to atomic resolution of the structure of a macromolecular system. Second, it is its ability to capture multiple conformational states of a protein with a single experiment. In the context of the S protein, the Cryo-EM technique reveal the RBD two distinct conformational states, up and down, that it can adopts.

Currently, Cryo-EM is particularly effective for large macromolecular complexes, but it presents certain limitations when applied to smaller proteins. Key challenges include a weaker signal-to-noise ratio (SNR), difficulty in particle alignment, and greater conformational flexibility. Proteins with a molecular weight below 100 kDa typically produce weak signals, making them more susceptible to image noise. Furthermore, they often lack distinct structural features, complicating accurate particle alignment during image processing. Additionally, their intrinsic flexibility can hinder the capture of a single, stable structure, making structural determination more challenging (Yeates et al., 2020).

With the aim to evaluate the antibody binding to RBD in both conformations and to overcome the Cryo-EM limitations linked to the molecular size of the examined sample, we expressed and purified the whole ectodomain of S protein and we used it to form a large complex with the humanized Fab useful for the Cryo-EM experiment that includes grid vitrification and data collection.

For the Single particle analysis, we followed the classical trial-and-error approach which is necessary to select only the best particles among the thousands or millions collected, that allow the high-resolution reconstruction of a density map of the object of interest.

For the sake of brevity and simplicity, here only the main and most significant steps of sample preparation and single particle analysis performed will be described.

4.1 Spike production and purification

Expi293 cells were transfected with the Spike HexaPro plasmid (addgene Plasmid #154754), a specific engineered version of the SARS-CoV-2 S protein, designed by Hsieh et al. for increased stability and improved expression in research setting (Hsieh et al., 2020). Indeed, S protein exists in a prefusion, metastable state on the surface of the SARS-CoV-2 virus but the six proline substitutions, introduced in Hexapro plasmid, make the protein more thermostable and resistant to denaturation, which helps maintaining its correct structure during expression and purification processes (Hsieh et al., 2020).

On the fourth day after transfection, the cell culture was centrifuged and the supernatant containing the protein was collected and diluted 1:2 with the equilibration buffer (10mM Tris pH 8, 20mM imidiazole and 500mM NaCl). A step of Ni-NTA chromatography followed by a SEC using a Superose6 Increase 10/300 GL column, were used to obtain a purified sample of the S protein.
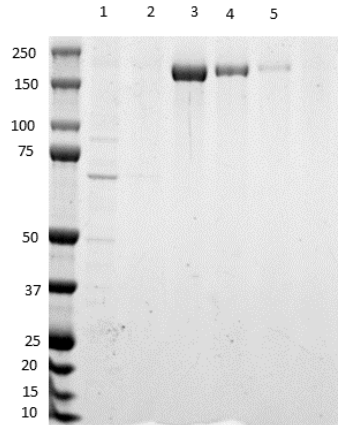
Figure 19: Hexapro S protein purification process. From left to right: flow through of Ni-NTA slurry resin (1), wash with 20 mM imidazole (2), first elution of 2 ml with 300 mM imidazole (3), second elution of 2 ml with 300 mM imidazole (4) and third elution of 2 ml with 300 mM imidazole (4). The denaturation induced by SDS and the presence of DTT enabled the isolation of the monomer of the S protein which corresponds to the single band comprise between 150 and 250 kDa, shown in the lanes 3, 4 and 5.

As shown in figure 19, the S protein was pure after the purification process. Indeed, we can see a single band between 150 and 250 kDa which corresponds to the S protein monomer. It is coherent with the estimated molecular weight for the HexaPro monomer that is around 200 kDa (Hsieh et al., 2020).

To remove any other components not visible on SDS page but present in the purified sample after affinity chromatography, we decided to further purify S protein using SEC. Furthermore, with this technique the native structure of S protein is maintain.

67
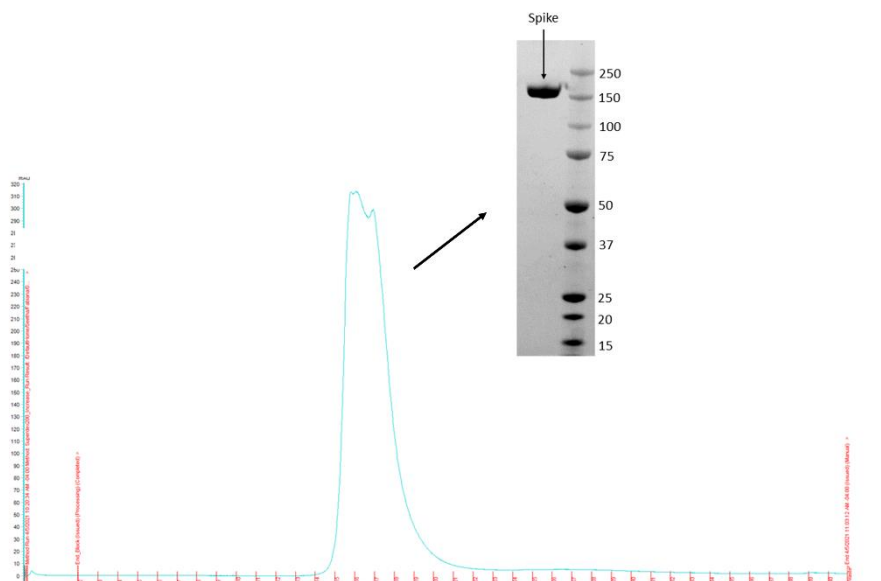
Figure 20: Hexapro S protein chromatogram. The peak corresponding to S protein collected is coloured in cyan. The SDS-page run of the peak fraction is also shown.

The elution volume of the peak is coherent with the molecular weight of S protein ectodomain (around 600 kDa).

4.2 Negative Staining Electron Microscopy (NS-EM)

We checked the homogeneity and the quality of the purified S protein by means of negative staining technique using transmission electron microscopy (NS-EM) at the Cryo-EM facility of CNB-CSIC (Madrid, Spain). These

experiments are critical for verifying protein integrity and structure prior to a more detailed and expensive analyses at the Cryo-EM microscope, providing a rapid and cost-effective method to assess the overall shape of the sample of interest.
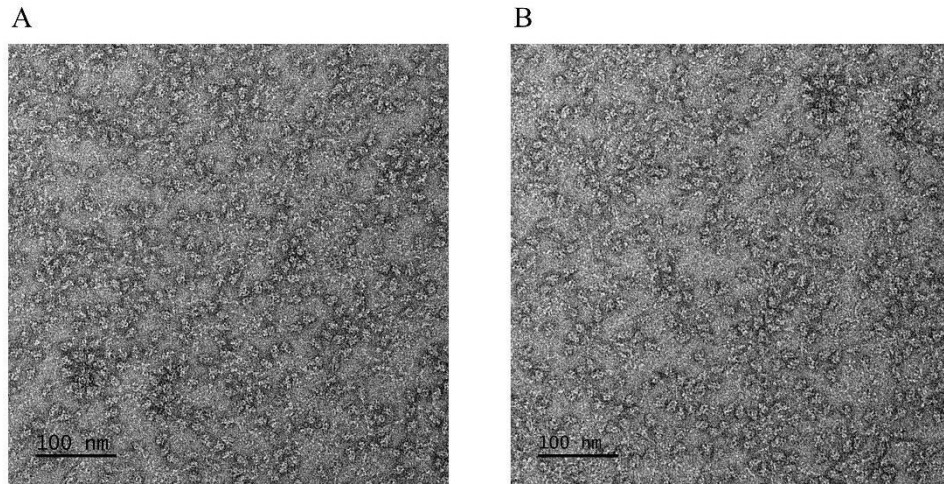
Figure 21: S protein NS-EM images. In figure A and B are shown different areas of the NS grid. The S protein appears homogeneous and evenly distributed.

While exploring various areas of NS grid, we observed that the S protein was well-distributed and exhibited a homogeneous appearance. No aggregates were detected. Although NS does not enable to reach high resolution reconstruction of a density map of the sample under study, it provides valuable information useful for the subsequent cryo-EM experiment, such as particle orientation. On this grid, we observed multiple orientations of the S protein, which is an essential factor to consider since it enables a complete (360°) reconstruction of a 3D structure.

69

4.3 Sample preparation and Cryo EM screening

Prior to collect cryo-EM data, a preliminary step of optimization of sample concentration, grid preparation and freezing conditions is usually carried out. We performed screening and data collection at the cryo-EM facility of the CNB-CSIC (Madrid, Spain). Freshly purified S protein was incubated with the humanized Fab to allow complex formation, as described in sections 8.2. Few microliters of sample were applied on glow-discharged Quantifoil® gold grids coated with a layer of carbon. An initial screening was performed to identify the best conditions of protein concentration and buffer. We found that a sample concentration of 1.2 mg/mL allowed an adequate number of particles to be deposited within the grid holes.

Eight different vitrification conditions were then tested, this time only varying the blotting force (as described in section 8.4), using a Vitrobot system. Screening was performed at the cryo-electron microscope using a FEI Talos Arctica 200 kV (Thermo Fischer Scientific). Ice thickness and particles distribution are the main aspects which are considered for the evaluation of the best vitrified grid, suitable for data collection. The grid blotted with blotting force 2 showed the best particle distribution and adequate ice thickness and it was used for an extended data collection.

4.4 Data collection and micrograph inspection

Using a multigrid data acquisition mode, a full dataset of 3372 movies (or micrographs) was collected using a Falcon 4i direct electron detector (Thermo Fischer Scientific). Micrographs were recorded in a low-dose mode to minimize the effects of radiation damage to the sample (1 e- /A2 per movie frame). A representative collected micrograph is showed in Figure 22. It displays a random and homogeneous distribution of particles in the vitreous ice layer, and the absence of ice contamination or significant particle aggregation reflects the good quality of the sample and of the vitrification procedure adopted. A pronounced background is observed, likely due to the presence of excess Fab that did not bind to the S protein. This unbound Fab increases noise in the micrographs.
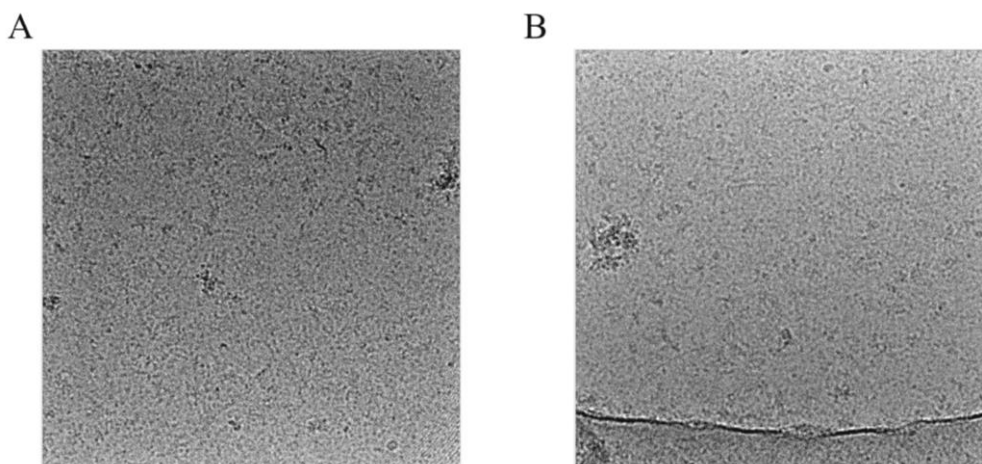
Figure 22. Inspection of typical cryo-EM micrographs of S protein and humanized 9-8F2-B11 Fab complex. Two representative micrographs from the data collection, showing the well-distributed particles of humanized 9-8F2-B11 Fab complex.

71

4.5 Single particle analysis

One of the biggest issues in Cryo-EM data analysis is the large computational resources required for single particle image processing and data storage, that cannot be sustained by a common personal computer. A typical cryo-EM data set is constituted by hundreds or thousands of images, each one being a movie of 2 gigabytes. Therefore, a single dataset consists of about 2 up to 5 TB of data that require at least 190 CPU-hours for each run of image processing. To speed-up the calculations, all software performing single particle analysis were implemented to use graphics processors (GPUs) to address the most computationally intensive steps of cryo-EM structure determination workflow. Therefore, the usage of GPU-based architecture is fundamental due to the highly demanding computational cost of a typical run of image processing.

To analyse the cryo-EM data we collected during my internship at CNB-CSIC, I worked in collaboration with the Instruct Image Processing Centre, I2PC (Madrid, Spain) who gave me the opportunity to use their IT resources thought Instruct ERIC access proposal (PID: 30541).

4.6 Image processing

Before working with single particles, images containing the 2D projections of the specimen of interest must be processed.

All data processing steps are performed with Scipion 3.0, developed by I2PC. This platform enables various tasks, such as particle sampling, 2D and 3D classification and refinement, by combining methods from different software packages such as Relion, CryoSPARC and Xmipp.

The 3372 movies collected were first aligned for beam-induced motion correction and drift with MotionCor2 (Zheng et al., 2017) then, CTF was calculated using CTFFIND4.1 (Rohou & Grigorieff, 2015). After an inspection of the whole data set, images containing relevant ice contamination or protein aggregation were removed and micrographs showing CTF resolution limits better than 5 Å were selected for further analysis.

Cryo-EM data analysis relies on a machine-learning approach, where, if manual selection is carried out, the human eye plays a crucial role in choosing the first set of particles from the collected micrographs to train the software in picking all the possible 2D projections resembling the specimen of interest. For S protein in complex with humanized Fab data set, 100 particles were manually picked from a selected group of micrographs with different defocus values and used as references for the automated particle picking procedure on the entire set of images. A total of 1,648,225 particles were collected and extracted from the original micrographs. From this point forward, all subsequent tasks were performed on these selected single particles.

4.6.1 2D classification

Extracted particles were subjected to a 2D classification, a procedure that classifies particles according to their shape and spatial orientation, generating

a certain number of 2D class averages containing views of differently orientated particles. The aim of the 2D classification step is to remove junk particles, contained in smeared or noisy classes that do not include the particles of interest, thus reducing their negative impact on the further steps of 3D reconstruction (Orlova & Saibil, 2011)

The 2D classification iteratively generated 300 class averages (K=100) from which we selected all the particles with have the typical shape of S protein bound to Fab (figure 23).
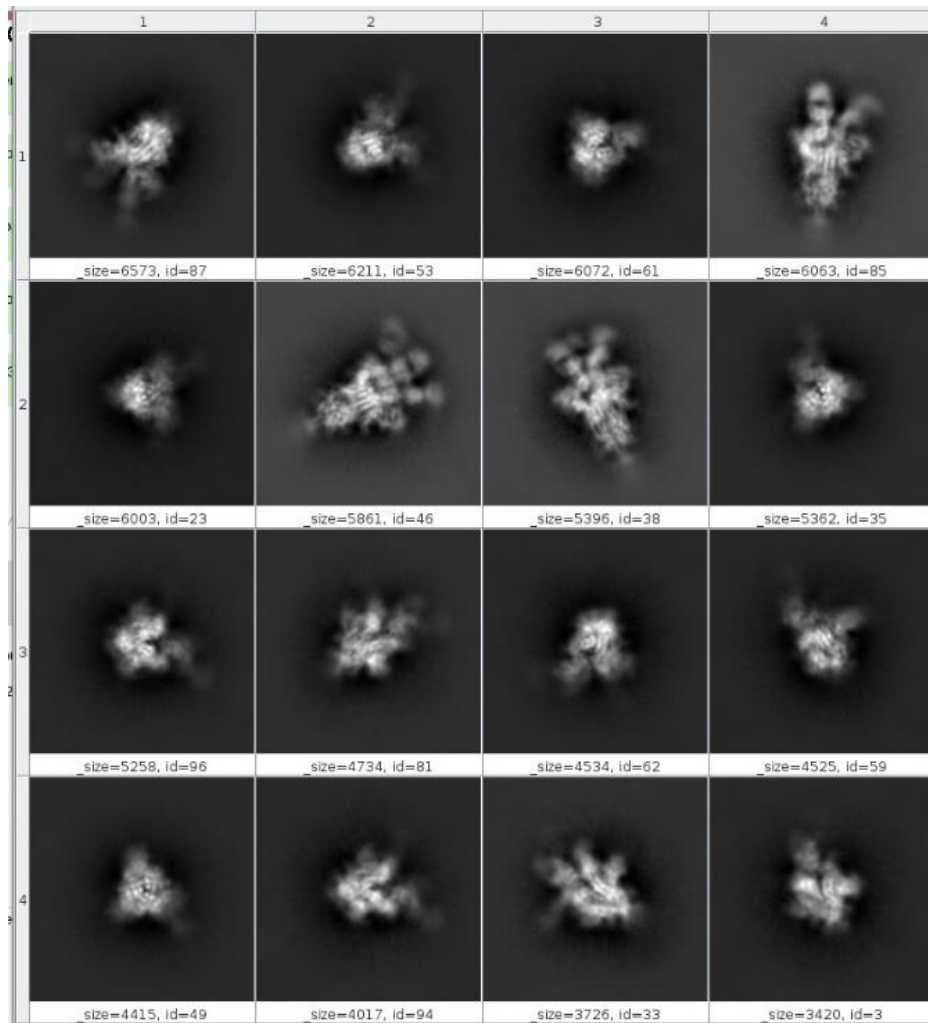
Figure 23. Best 2D class averages resulted by 2D classification performed using CryoSPARC in Scipion 3.0.

As shown in figure 23, the 2D classes showed two promising features, mandatory for achieving high resolution maps: 1) secondary structure elements

are clearly discernible and 2) particles show a variety of orientations, indicating a good coverage in the projection sphere.

4.6.2 Generation of a 3D initial model, 3D classification and 3D refinement

A preliminary low resolution three-dimensional map of S protein- humanized Fab complex was generated using the 3D Ab Initio Model tool in Cryosparc available in Scipion 3.0. This map providing a first clue on the architecture of the complex, even if was not possible to detect any detailed structural information, being the map at low resolution. We started by finding six 3D initial models based on the possible conformations of the sample and the most representative and detailed one was selected.
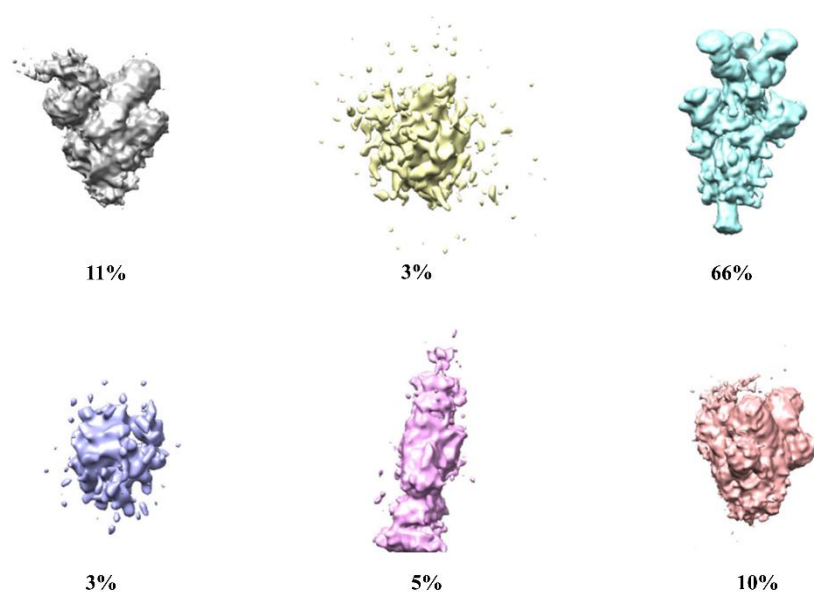
Figure 24. Cryo EM Ab initio models. The cyan map is most populated. The percentage refers to the number of particles from the 2D classes that were used to generate the volumes corresponding to the relative 3D class.

The most populated 3D class map was refined with C3 symmetry using the CryoSPARC non-uniform refinement tool. To improve the accuracy of the map and explore different RBD conformations, we performed 3D autorefinement and local refinement in Relion. During these steps, symmetry was released by imposing no symmetry (C1), allowing the map to more accurately capture asymmetric variations in the structure. Following this, the map was used as input for 3D flex correction, using 3D flex refinement tool available in Cryosparc. This technique was designed to address conformational flexibility within macromolecular complexes

77

(Beckers et al., 2021). Traditional 3D refinement methods tend to average different conformational states, resulting in blurred regions in the final map. Flexibility correction allows the identification and refinement of these distinct conformations separately, which is particularly important for our sample, where it is well know the RBD flexibility (Dokainish et al., 2022). Analysis of this refined cryo-EM map revealed that two RBDs are in a down conformation, while the third RBD is in an up conformation. Based on this initial structural information, this corrected and refined map was also used for additional refinement cycles, performed applying masks focused on either the RBD-down-Fab and RBD-up-Fab regions. This approach was critical for improving the resolution at the RBD-Fab interface, enabling us to better identify the epitope recognized by the humanized antibody. The refined maps were then improved and sharpened using the post-processing tool, crucial for enhancing the quality and resolution of 3D reconstructions after the initial refinement steps. This sharpening refinement improves map detail by emphasizing high-resolution features (Sanchez-Garcia et al., 2021). The maps obtained during the vary refinement are shown in the following figure.

3.6 Å

Post-3D Autorefinement e local refinement map (Relion)

Post-3D Flex Refinement.(Cryosparc)

RBD down – Fab Masked map

RBD up – Fab Masked map

Post-processed sharpening

3.9 Å

4.1 Å
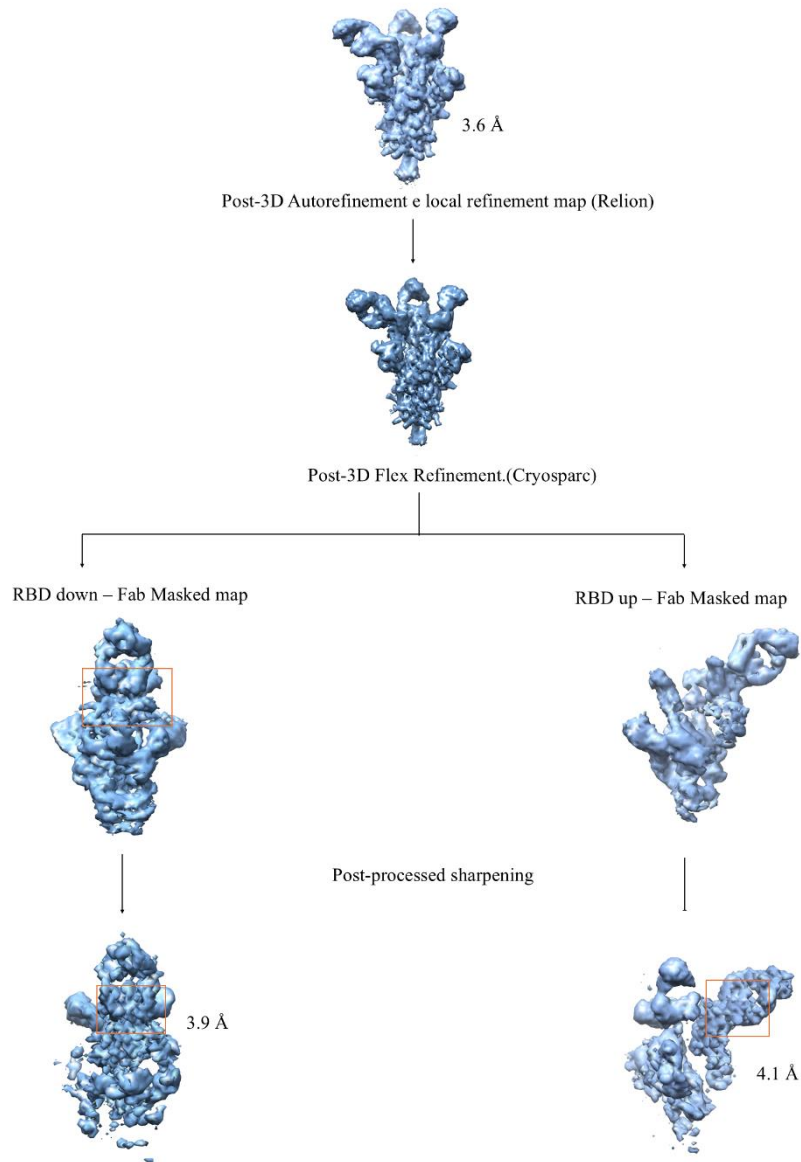
Figure 25. Cryo EM map optimization step-by-step. The maps obtained by masking the RBD-Fab interfaces have a red square indicating the contact zone. The global resolution of each map is reported.

79

The global (average) resolution of the map obtained after 3D local refinement and the maps obtained by masking the RBD down-Fab and RBD up-Fab interfaces are 3.6 Å, 3.9 Å and 4.1 Å respectively.

The global resolution has a potential limitation since it does not account for local variations in resolution, which can arise from processing errors or data heterogeneity, especially in the analysis of macromolecular complexes. Analysing local fluctuations in resolution across different areas of the structure is crucial for guiding the construction of a 3D atomic model within Cryo-EM maps, helping to avoid misinterpretation of poorly defined densities. For the sample under investigation, it is essential to understand the resolution distribution, particularly in the map obtained by masking the RBD-Fab interfaces, to accurately interpret binding interactions. With this aim, we employed the xmipp3 Local Resolution tool implemented in Scipion 3.0, to investigate how resolution is distributed throughout the density map for both the RBD down-Fab and RBD up-Fab complexes.

A   B

RBD down - Fab   **RBD up - Fab**
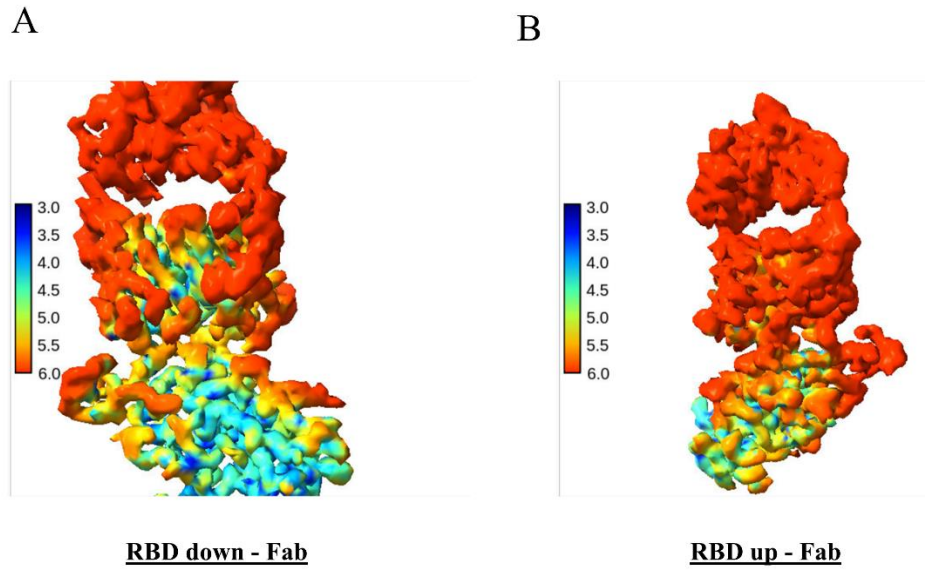
Figure 26. Local resolution of the RBD down – Fab masked map (A) and the RBD up – Fab masked map (B). The maps are coloured according to local resolution, with a gradient ranging from red to blue representing the region with higher and lower resolution, respectively.

Analysing the local resolution fluctuations in these maps, we determined that the resolution at the RBD-Fab interfaces varies from 4 to 4.5 Å, with the RBD down-Fab pair showing higher resolution due to its higher stiffness. At both interfaces, the secondary structures and bulky side chains of the interacting residues are clearly visible, providing better structural detail.

4.6.3 Model building

The first step in model building involves performing a rigid body fit of the existing structural model using Chimera. For this purpose, the initial model of the previously deposited structure of the S protein (PDB: 7FB1) and the Fab structure predicted using AlphaFold were manually positioned within the density map of the overall structure, which had been sharpened following post-processing. For the maps obtained with focused masks at the interface, only a single RBD of S protein and one Fab was used for the rigid body fit. To refine the atomic model at the individual atom level, the Real Space Refinement tool in Phenix was employed (Afonine et al., 2018). Following this, the map and the refined atomic model were further processed in Coot, a program that allows for manual adjustment and refinement of the atomic model within the density map. The first model building steps for each map obtained during data processing are summarised in Figure 27.
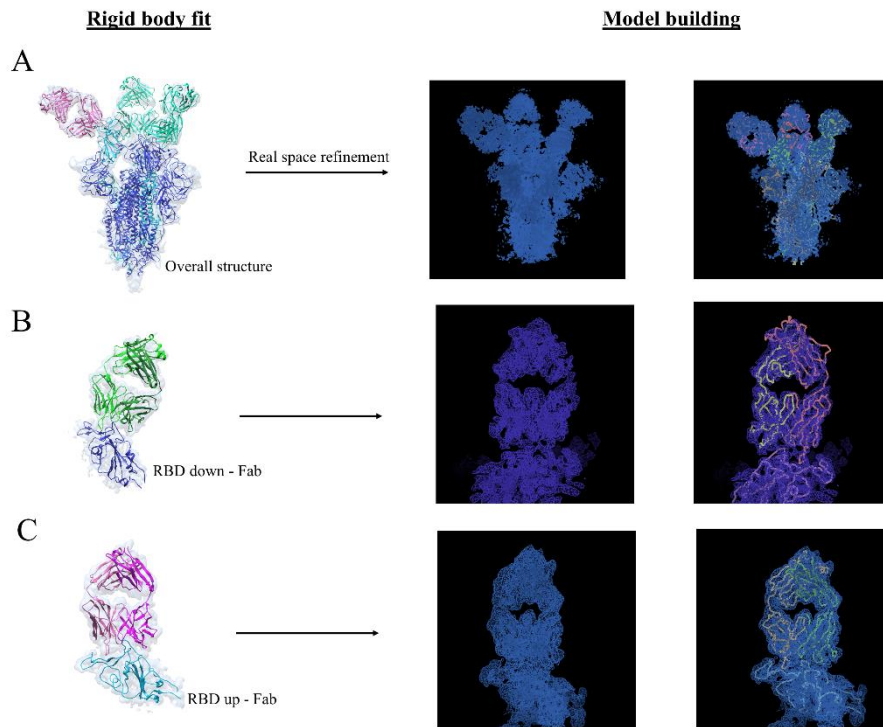
Figure 27. Model building of S protein in complex with Fab (A), RBD down-Fab (B) and RBD up-Fab. The protomer with the RBD in the down conformation is displayed in blue, while the protomer with the RBD in the up conformation is shown in cyan. The two Fabs bound to the RBD-down conformation are coloured in green, and the Fab bound to the RBD-up conformation is represented in pink.

We manually refined the model, focusing primarily on adjusting the CDRs of the Fab and RBD, which initially did not fit well within the Cryo-EM map as shown in the figure 28.

83
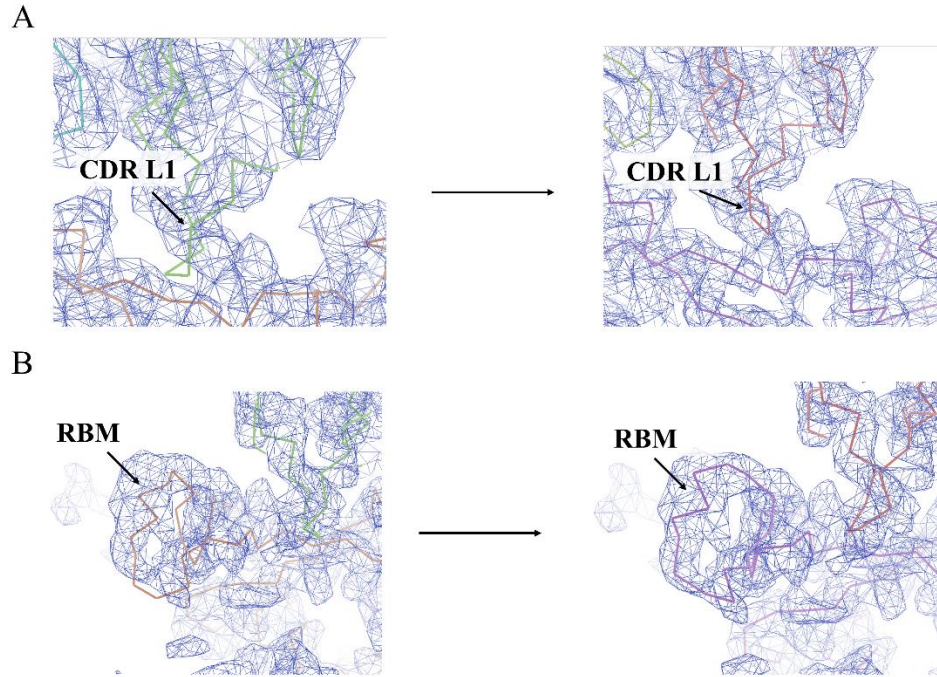
Figure 28. CDR and RBD manual refined on Coot. An example of CDR L1 (A), CDR and RBD (C) are shown. On the left, the model obtained from the real space refinement with phenix. On the right, the model manually refined with coot.

4.7 Structural analysis of S protein in complex with the humanized Fab

The Cryo-EM structure of the S protein in complex with the humanized 9-8F2-B11 Fab revealed that three Fab fragments are bound to the RBD of the S protein in a heterogenous conformation: one Fab is attached to the RBD in its up conformation, while the other two are bound to the RBD in its down conformation. Figure 29 illustrates the overall structure of the complex and a

detail of each S protein protomer fitted to corresponding Cryo-EM density map.

one RBD-up, two RBDs-down configuration

RBD up   RBD down   RBD down
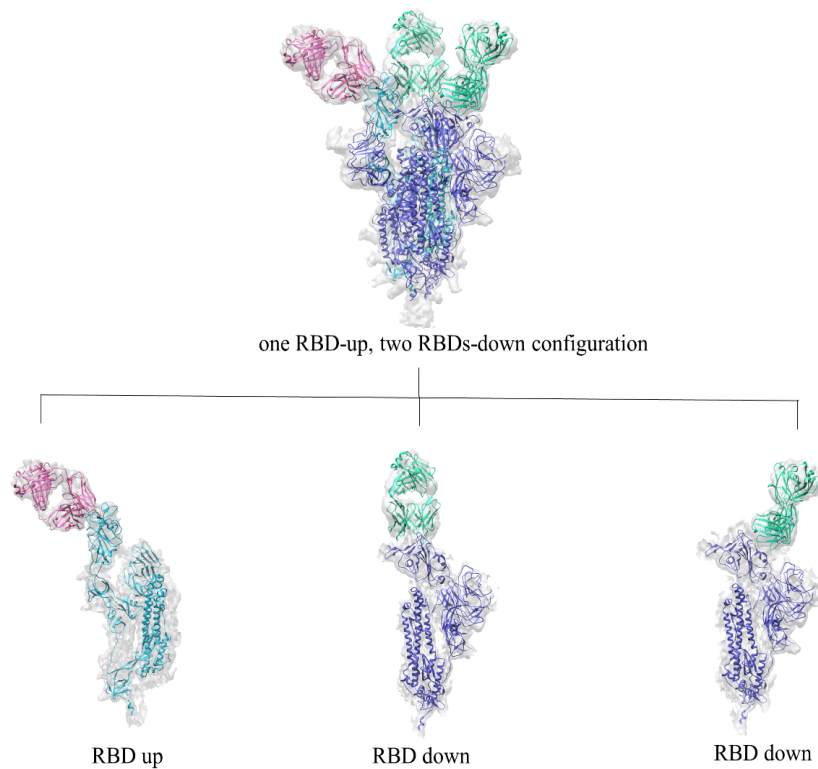
Figure 29: The overall structure of Spike-Fab complex fitted into their relative cryo-EM maps (light grey). Each monomer are shown individually in order to provide a clear depiction of the Fab positioning relative to the specific RBD conformation: one S monomer has RBD in the up state and the other two monomers present their RBD in the down state. The protomer with the RBD in the down conformation is displayed in blue, while the protomer with the RBD in the up conformation is shown in cyan. The two Fabs bound to the RBD-down conformation are coloured in green, and the Fab bound to the RBD-up conformation is represented in pink. The image is created with UCSF Chimera

As previously described, many NAbs recognize epitopes on the RBD that are exposed only when it is the up state. Indeed the ability of the RBD to adopt a

down conformation helps generally enables these epitopes to be concealed, preventing NAbs recognition or binding (Pipitò et al., 2022). Therefore, the observation that the humanized antibody under investigation is capable of binding the RBD in both its up and down conformations represents a significant achievement highlighting its valuable therapeutic potential against SARS-CoV-2.

Based on the classification of NAbs by their epitope recognition reported by Deshpande et al., 2021, we can conclude that the humanized 9-8F2-B11 belongs to the second class, which includes NAbs capable of binding the RBD in both up and down conformations.

4.7.1 Epitope characterization

Thanks to the 4Å resolution cryo-EM map obtained by masking the interfaces, we were able to reconstruct an accurate atomic model covering these areas. We have identified the epitope of the humanized 9-8F2-B11 Fab, which is a region within the RBM of the RBD. Surprisingly, the comparison between the RBD down-Fab and RBD up-Fab complexes showed no significant differences in the antibody-recognized region. Therefore, we attributed the Fab ability to bind the RBD even in its down conformation to the recognition of a specific region within the RBM that remains exposed even when the RBD is in this conformation, as illustrated in Figure 30.
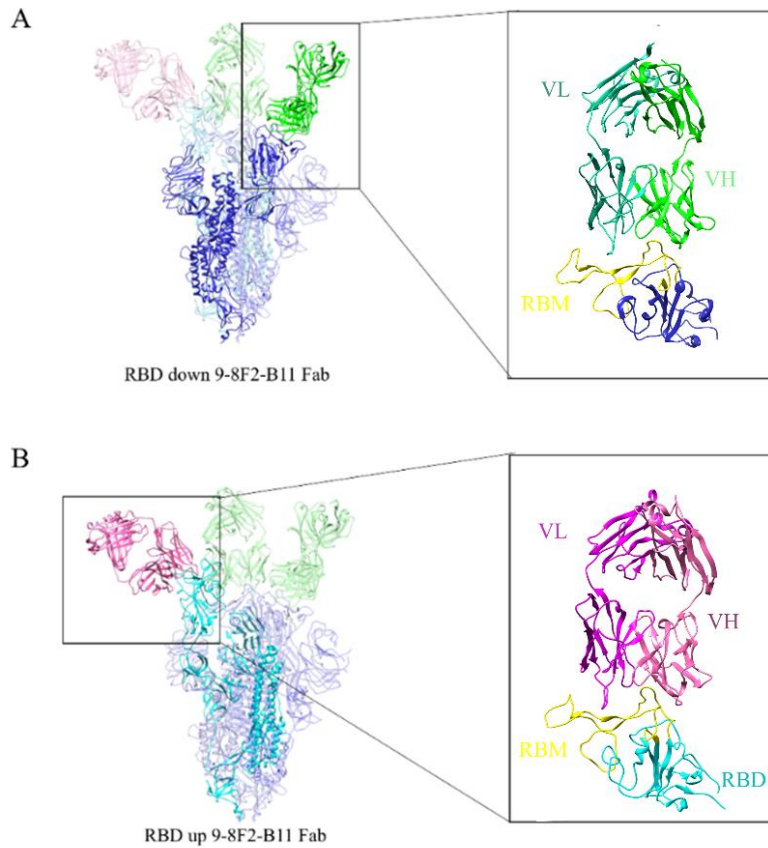
Figure 30. RBD down-Fab (A) and RBD up – Fab (B) structures comparison. The monomer with the RBD in the down conformation is depicted in blue, while the monomer with the RBD in the up conformation is shown in cyan. The corresponding bound Fab fragments are represented in green and pink, respectively. The overall structure of the S protein bound to the Fab fragments is displayed with transparency. Enlarged views of the interfaces are provided in the panels, allowing a clearer visualization of the Fab orientation, which remains consistent between the two conformations.

87

More in details, humanized 9-8F2-B11 has one conformational epitope. The interface residues of RBD and Fab exposed are approximately the same for RBD down and up (Figure 31). They were determined using PDBePISA tool which is based on changes in solvent-accessible surface area (ASA) when two proteins form a complex (Krissinel & Henrick, 2007). For the down-Fab RBD structure obtained with a higher resolution map (~4Å), this analysis showed that: the interaction surface was $902Å^2$, and both chains contribute equally to the interaction with the antigen; in particular, the light chain (C chain) interacts on a $495Å^2$ surface, while the heavy chain (B chain) interacts on a $407Å^2$ surface.

The heavy and light chain CDRs in both interfaces interact closely with residues in the RBM region between T345 and T500. More in detail, the residues of RBD at the interface with the humanized 9-8F2-B11 Fab fragment are: 345-346, 440-452, 455-456, 472, 483-E484, 486, 489, 490-494 and 498-500.
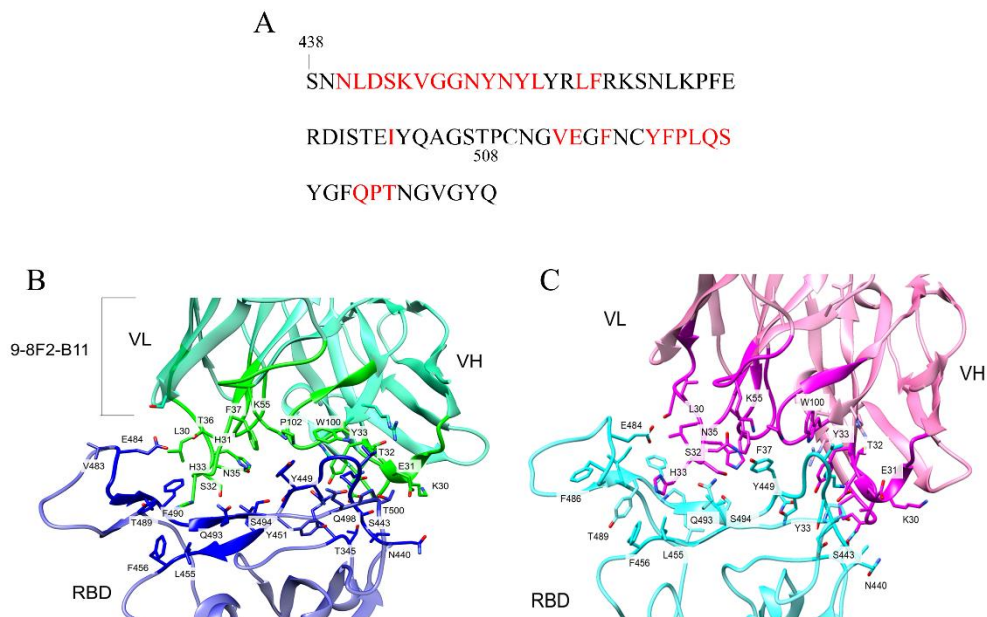
Figure 31. Epitope characterization of humanized 9-8F2-B11 Fab. (A) RBD sequences with the red residues corresponding to 9-8F2-B11 epitope. Interface residues of RBD down – Fab (B) and RBD up-Fab (C) are shown in sticks. The Fab CDR are in light green while the framework regions are in dark green. In the figure B the Fab CDR are in magenta while the framework regions are in pink.

The RBD down–Fab structure shows a better resolution at the interface (~4 Å), as detailed in section 4.6.3, enabling an accurate identification of hydrophobic interactions, which involve aromatic amino acids with bulky side chains. The hydrophobic interactions involve W100 of Fab VH3 with V449 of the RBD, and F37 of Fab VL1 with Y499 of the RBD (figure 32A).

Despite the limited atomic detail provided by the resolution, an interface analysis was performed and some interactions, including hydrogen bonds and

89

salt bridges, were inferred based on the proximity of the residues. Here follows a more detailed description: two salt bridges are likely formed between D57 of VH and R346 of the RBD. Hydrogen bonds are inferred between the backbone carbonyl group of RBD V445 and the backbone amine group of E31 of the Fab, while RBD K444 appears to interact with the carbonyl group of G101. Additional hydrogen bonds, involving only the side chains, are predicted between i. RBD N448 and Fab T33, ii. RBD T345 and E57 of Fab, iii. R346 of RBD and E57 of Fab. The contacts between the Fab VL and RBD include a hydrogen bond between the backbone carbonyl group of RBD L492 and the backbone amine group of Y33. Side chain interactions include contacts between the aa of RBD and Fab: Y449 and K55, E484 and T36, and R493 and H33. These interactions are shown in figure 33 C and D for the VH and VL, respectively.
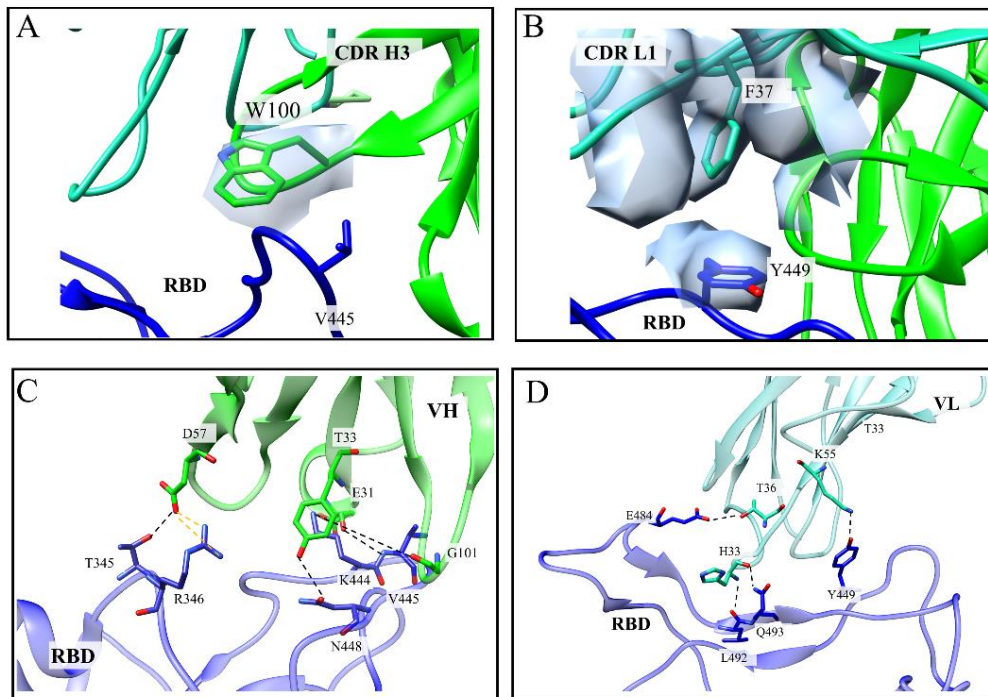
Figure 32. RBD and 9-8F2-B11 Fab: interacting residues. The residues involved in the interaction are labelled and represented in sticks. In the panels A and B, the hydrophobic interactions are shown fitted into the Cryo EM map, shown as a light blue surface. In the panels C and D some putative hydrogen bonds (black) and two salt bridges (orange) are represented by dotted line.

4.7.2 Structural comparison between RBD-ACE2 and RBD-Fab interfaces

The pseudovirus neutralization assay demonstrated that the humanized antibody 9-8F2-B11 effectively prevents viral entry into host cells (figure 14). The Cryo-EM structure revealed that the antibody recognizes an epitope within

the RBM region, which partially overlaps with the area involved in the RBD-ACE2 interaction. The superimposition of the RBD-ACE2 (PDB: 6M0J) and RBD up – 9-8F2-B11 Fab structures revealed that the VH of Fab and the PD domain of ACE2 partially recognize the same region of RBM, providing structural explanation for the observed competition between the antibody and ACE2, as shown in figure 33.
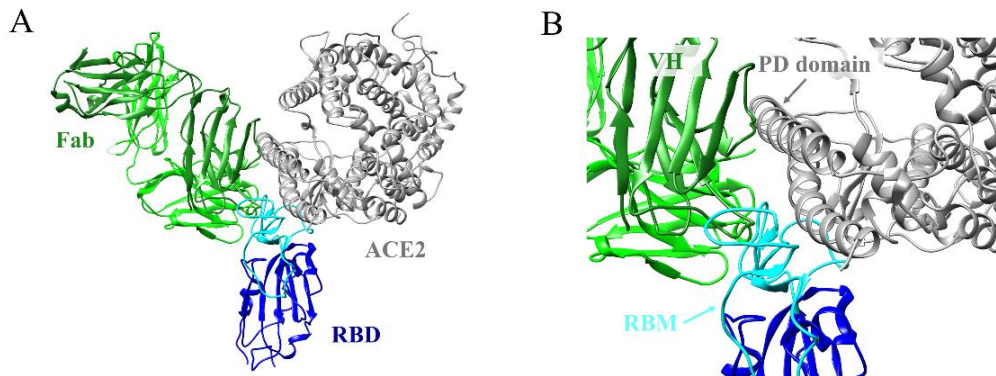
Figure 33: Superimposition between ACE2-RBD and Fab-RBD structures. The ACE2-RBD structure (PDB:6M0J) is superimposed with Fab-RBD structure solved in this work. ACE2 and Fab are colored in violet and green, respectively. RBD is in blue and light green for RBD-ACE and RBD-Fab1, respectively. The image was created with UCSF Chimera.

Indeed, the RBD interface residues showed in figure 35A (Y449, L455, F486, Q498 and T500) which are involved in the ACE2 binding are also recognized by the Fab, preventing the ACE2-RBD binding with a direct mechanism. Nevertheless, some residues of RBD are specific for the Fab binding, as shown in figure 34 (panels B and C).

The presence of a different pattern of interacting residues for the Fab and ACE2 determine the different orientation adopted by the two partners towards the RBD, as shown in Figure 33 and 34A.
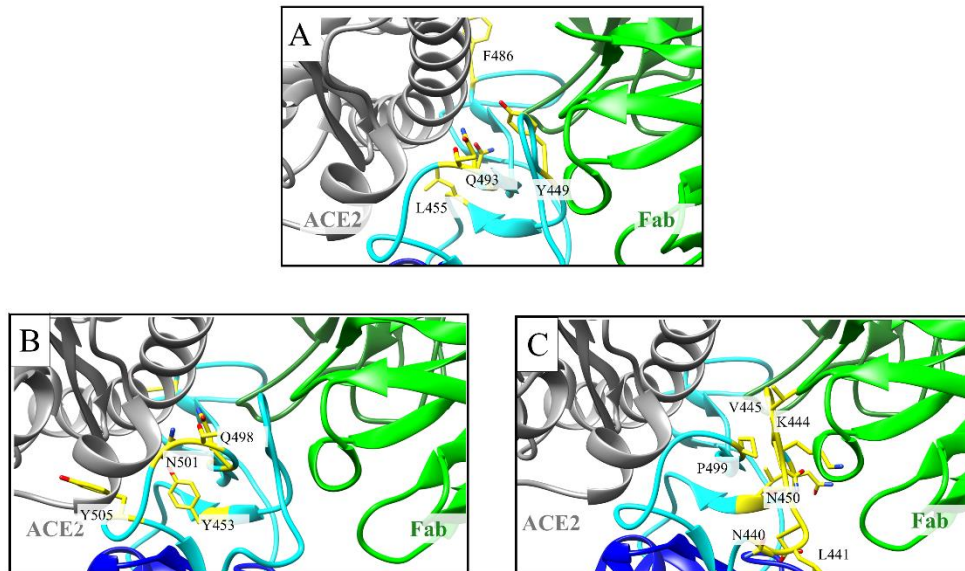
Figure 34: Comparison of RBD-ACE2 and RBD-Fab interface. In the panel A the interface residues shared between the Fab and ACE2 are represented in yellow sticks. In the other two panels the unique interface residues for ACE2 (B) and Fab (C) are represented.

Furthermore, The affinity of the wild type RBD for ACE2, as measured by BLI, is approximately 15 nM (Haycroft et al., 2023), which is 6.8-fold lower than the affinity measured for the Fab fragment (~2.2 nM). The increased affinity enhances Fab binding to the RBD, making it more competitive than ACE2.

The competition mechanism with ACE2, together with the ability of Fab 9-8F2-B11 to bind both states of RBD, allows the humanized antibody to directly block ACE2 recognition and to be active on a RBD state where common antibodies lose efficacy.

5. Comparison between chimeric and humanized 9-8F2-B11

Differences in affinity and activity of chimeric and humanized antibodies have been demonstrated. In both chimeric and humanized antibody, the constant regions (CL and CH1) come typically from a human antibody framework, facilitating compatibility with human immune systems. In the chimeric antibody the CDRs belonging to the variable domain present the murine scaffold while in the humanized antibody these regions present the human scaffold. The humanization process is crucial if the aim is the human treatment with antibody. Indeed, the human framework regions reduce the possibility to induce immunogenicity in human (Chiu et al., 2019). The primary drawback of modifying the framework region is that such changes can adversely affect the conformation and orientation of the CDR, which are crucial for antigen binding. When alterations are made to the framework regions, even subtle changes can lead to a shift in the spatial arrangement of the CDRs. This misalignment can hinder the ability of the antibody to effectively bind its target, potentially diminishing its biological activity. Additionally, if the changes result in an unfavourable conformation, the antibody may lose its

94

stability, affecting its overall efficacy and therapeutic potential (Almagro et al., 2018).

In the figure 35, the sequences alignment, performed with Blast (McGinnis & Madden, 2004), shows the amino acids differences in both 9-8F2-B11 VH and VL between chimeric and humanized antibody.


Figure 35: Chimeric and humanized amino acids Fab sequences alignment. The alignment of Fab VH (A) and Fab VL (B) is shown. The VH and VL of humanized and chimeric antibody are highlighted in yellow and green respectively. The CDRs are highlighted with a red square.

With the aim to elucidate the structural reasons behind the observed differences in affinity and activity between chimeric and humanized 9-8F2-B11, a structural characterization of the complex formed between the S protein bound to chimeric 9-8F2-B11 Fab by Cryo EM was pursued. Here follows the description of the sample preparation, data collection and data processing and preliminary results.

5.1 Cryo EM sample preparation and data collection

Cryo-EM grids of the chimeric 9-8F2-B11 Fab and S ectodomain were vitrified using the same conditions identified for the humanized Fab-S protein complex. In this case, a sample concentration of 1.2 mg/ml was used. Upon examination of the cryo-EM micrographs, it was observed that only a few particles resembling the S protein were located near the edges of the holes. Additionally, the presence of an excess of Fab was clearly noticeable if compared to the humanized Fab-S protein complex images, contributing to an enhanced signal from the background (Figure 36).
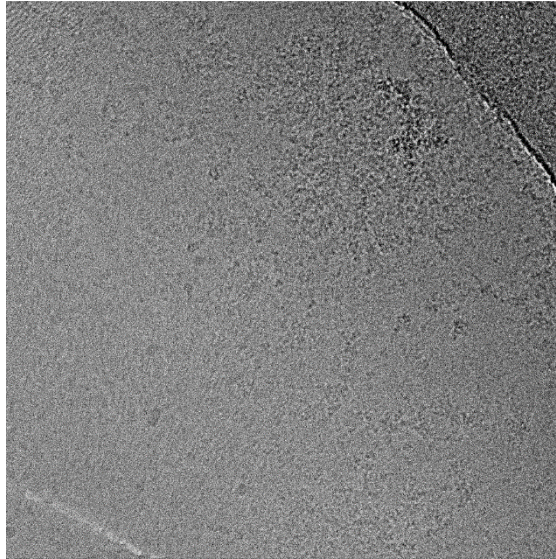
Figure 36: Representative micrograph of chimeric 9-8F2-B11 Fab bound to the S protein.

A small data collection was carried out at the CNB-CSIC (Madrid, Spain). The data collection parameters are summarized in table 1.

## 5.2 Preliminary Cryo EM data processing of chimeric 9-8F2-B11 in complex with S protein

The preliminary Cryo EM data processing of chimeric 9-8F2-B11 Fab and S protein was performed using CryoSparc. Micrographs (~1900) were imported and the CTF estimation was carried out. A preliminary particles selection was carried out using blob picker tool, which works by identifying regions of high signal intensity. Particle picking identified ~811,677 particles that were

97

extracted, using a box size of 415 that was rescaled to 200, and classified in 2D classes. The best 2D class was used for the template picking procedure, in which particle projections generated from prior processing step are used as templates for identifying and selecting similar particles in new micrographs. Five rounds of 2D classification were carried out to clean the data set by removing particles of no interest. In this case, many of the 2D classes contained particles that did not have the typical shape of the Fab-bound S protein. These small particles could be due to the excess of Fab used. Anyway, a 3D ab initio model reconstruction was performed selecting the best 2D classes shown in figure 37B. In some of them it is possible to observe the secondary structure of the helices that form the S2 subunit of the S protein. This region is not flexible and usually it is easier to visualize.
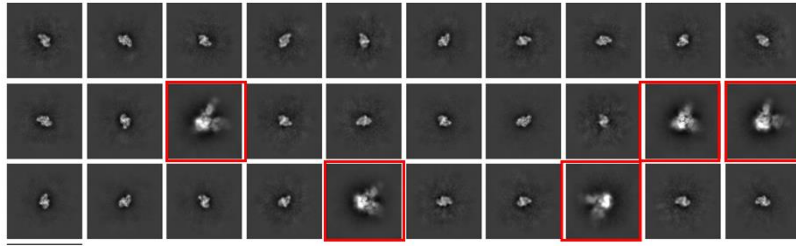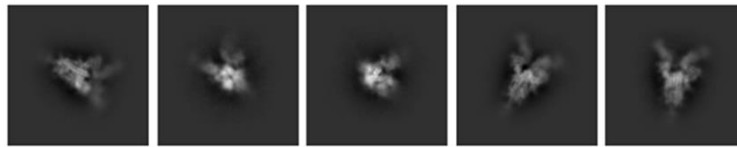
F**igure 37: 2D classes of chimeric 9-8F2-B11 Fab bound to the S protein.** In panel A, the 2D classes obtained from the first 2D classification are shown. The 2D classes containing particles with a shape like S protein bound to Fab are highlighted with a red square. In panel B are shown the 2D classes chosen for the Ab initio model reconstruction.

Despite the small number of particles (~ 9,205), ab initio model was obtained and refined using non-uniform refinement tool of CryoSparc.

A   B
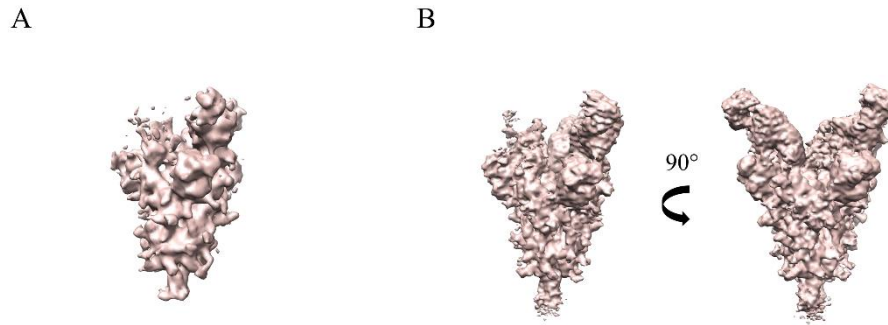
Figure 38. 3D models of chimeric 9-8F2-B11 Fab in complex with S protein. In the figure A, the ab initio model is shown. Two different views of refined map are shown in the figure B.

At the first glance, the reconstructed map appears to show two RBDs in the up conformation, each bound to an Fab. The third protomer, however, seems to be unbound.

Although the global resolution estimated during the refinement was around 5.5 Å, attempting a rigid body fitting fit of an atomic model of Fabs and the S protein was unsuccessful, as the model could not be accurately positioned into the density. For this reason, we decided to vitrify new Cryo EM grids using a reduced amount of Fab to facilitate the formation of the complex and a more entended data collection was carried out (CNB-CSIC, Madrid, Spain). Data processing in still ongoing.

Conclusions and future perspectives

The primary focus of this study was to evaluate the efficacy of the humanized 9-8F2-B11 antibody *in vitro* and to elucidate the fundamental interactions between this high-affinity monoclonal antibody, developed by Takis S.r.l., and the S protein RBD. Indeed, SARS-CoV-2 S protein is the primary factor responsible for initiating infection in humans. This protein facilitates the virus's entry into host cells by binding to the ACE2 receptor exposed to the surface of cells, particularly in the respiratory system. Once attached, the virus can fuse with the cell membrane and release its genetic material inside the host cell, leading to the replication of the virus and the progression of COVID-19.

In this study, we demonstrated that humanized 9-8F2-B11 binds to the RBD viral strains with high specificity, as evidenced by the K_D values ranging between ~1.4 nM and ~ 6 nM for all the RBD variants tested, with the exception of the Beta and Omicron BA.1 variants, which exhibit a K_D of approximately 18 nM.

Furthermore, *in vitro* studies showed that the humanized antibody can block SARS-CoV-2 entry into host cells with a ND50 comparable with the ND50 values obtained with antibodies identified by convalescent patients, such as Sotrovimab.

We have determined a Cryo-EM structure of the 9-8F2-B11 Fab in complex with the S protein at ~4Å resolution. The structure demonstrates that the humanized 9-8F2-B11 Fab binds the RBD in both down and up conformations.

This is a promising result, as the down conformation of the RBD typically hinders antibody recognition.

The structure also revealed that the humanized 9-8F2-B11 antibody competes with ACE2 in RBD binding site since it recognizes key residues ate the RBM domain, which are critical for ACE2 interaction.

The multiple advantageous characteristics of this antibody, namely its competition with ACE2, its recognition of the RBD domain in the down conformation, and its ability to neutralize all SARS-CoV2 variants (except BA.1), make its usage promising for the treatment of viral infection. Furthermore, the knowledge of the epitope recognized by the humanized 9-8F2-B11 and its intrinsic broadly neutralization mechanism make this antibody an ideal candidate for the rational engineering towards new emerging variants such as XEC, JN.1, and FLiRT, which are becoming increasingly common in 2024. With this future perspective, we are planning to investigate how single mutations belonging to SARS-CoV2 variants affect antibody recognition.

The second aim of this study was to compare the affinity, activity, and structural characteristics of the humanized and chimeric 9-8F2-B11 antibodies. While it is well-established that humanizing antibodies often results in reduced efficiency, understanding how alterations in the framework regions affect the conformation and orientation of the CDRs is crucial. Such insights are particularly valuable for companies like Takis Biotech, which are specialized in generating antibodies using hybridoma technology. Since murine-derived antibodies require humanization to minimize immunogenicity for therapeutic use, revealing these structural differences could aid in optimizing the humanization process in order to retain or enhance antibody function.

Unfortunately, in this work, we were not able to determine a high-resolution Cryo-EM structure of the chimeric Fab-antigen complex, and the work is still ongoing. A larger Cryo-EM dataset is currently being processed. Once the image processing is completed, a detailed comparison between the chimeric and humanized structures will be performed to uncover the structural adaptations that occur during the humanization process. This knowledge will be instrumental to develop alternative humanized antibodies that maintain or even improve their therapeutic efficacy.

Bibliography

Afonine, P. V., Poon, B. K., Read, R. J., Sobolev, O. V., Terwilliger, T. C., Urzhumtsev, A., & Adams, P. D. (2018). Real-space refinement in PHENIX for cryo-EM and crystallography. Acta Crystallographica Section D: Structural Biology, 74(6), 531–544. https://doi.org/10.1107/S2059798318006551

Almagro, J. C., Daniels-Wells, T. R., Perez-Tapia, S. M., & Penichet, M. L. (2018). Progress and challenges in the design and clinical development of antibodies for cancer therapy. In Frontiers in Immunology (Vol. 8, Issue JAN). Frontiers Media S.A. https://doi.org/10.3389/fimmu.2017.01751

Bai, C., Zhong, Q., & Gao, G. F. (2022). Overview of SARS-CoV-2 genome-encoded proteins. *Science China Life Sciences*, *65*(2), 280–294. https://doi.org/10.1007/s11427-021-1964-4

Bai, H., Zhang, X., Gong, T., Ma, J., Zhang, P., Cai, Z., Ren, D., & Zhang, C. (2024). A systematic mutation analysis of 13 major SARS-CoV-2 variants. *Virus Research*, *345*. https://doi.org/10.1016/j.virusres.2024.199392

Cai, Y., Zhang, J., Xiao, T., Peng, H., Sterling, S. M., Walsh, R. M., Rawson, S., Rits-Volloch, S., & Chen, B. (2020). Distinct conformational states of SARS-CoV-2 spike protein. *Science*, *369*(6511). https://doi.org/10.1126/science.abd4251

Chang, C. ke, Chen, C. M. M., Chiang, M. hui, Hsu, Y. lan, & Huang, T. huang. (2013). Transient Oligomerization of the SARS-CoV N Protein - Implication for Virus Ribonucleoprotein Packaging. *PLoS ONE*, *8*(5). https://doi.org/10.1371/journal.pone.0065045

Cheng, L., Song, S., Zhou, B., Ge, X., Yu, J., Zhang, M., Ju, B., & Zhang, Z. (2021). Impact of the N501Y substitution of SARS-CoV-2 Spike on neutralizing monoclonal antibodies targeting diverse epitopes. *Virology Journal*, *18*(1). https://doi.org/10.1186/s12985-021-01554-8

Chiu, M. L., Goulet, D. R., Teplyakov, A., & Gilliland, G. L. (2019). Antibody structure and function: The basis for engineering therapeutics. In Antibodies (Vol. 8, Issue 4). MDPI. https://doi.org/10.3390/antib8040055

D'Acunto, E., Muzi, A., Marchese, S., Donnici, L., Chiarini, V., Bucci, F., Pavoni, E., Ferrara, F. F., Cappelletti, M., Arriga, R., Serrao, S. M., Peluzzi, V., Principato, E., Compagnone, M., Pinto, E., Luberto, L., Stoppoloni, D., Lahm, A., Groß, R., … Roscilli, G. (2024). Isolation and Characterization of Neutralizing Monoclonal Antibodies from a Large Panel of Murine Antibodies against RBD of the SARS-CoV-2 Spike Protein. Antibodies, 13(1). https://doi.org/10.3390/antib13010005

Davidson, A. D., Williamson, M. K., Lewis, S., Shoemark, D., Carroll, M. W., Heesom, K. J., Zambon, M., Ellis, J., Lewis, P. A., Hiscox, J. A., & Matthews, D. A. (2020). Characterisation of the transcriptome and proteome of SARS-CoV-2 reveals a cell passage induced in-frame deletion of the furin-like cleavage site from the spike glycoprotein. *Genome Medicine*, *12*(1). https://doi.org/10.1186/s13073-020-00763-0

de Souza, A. S., de Souza, R. F., & Guzzo, C. R. (2023). Cooperative and structural relationships of the trimeric Spike with infectivity and antibody escape of the strains Delta (B.1.617.2) and Omicron (BA.2, BA.5, and BQ.1). *Journal of Computer-Aided Molecular Design*, *37*(12), 585–606. https://doi.org/10.1007/s10822-023-00534-0

Dejnirattisai, W., Zhou, D., Supasa, P., Liu, C., Mentzer, A. J., Ginn, H. M., Zhao, Y., Duyvesteyn, H. M. E., Tuekprakhon, A., Nutalai, R., Wang, B., López-Camacho, C., Slon-Campos, J., Walter, T. S., Skelly, D., Costa Clemens, S. A., Naveca, F. G., Nascimento, V., Nascimento, F., … Screaton, G. R. (2021). Antibody evasion by the P.1 strain of SARS-CoV-2. *Cell*, *184*(11), 2939-2954.e9. https://doi.org/10.1016/j.cell.2021.03.055

Deshpande, A., Harris, B. D., Martinez-Sobrido, L., Kobie, J. J., & Walter, M. R. (2021). Epitope Classification and RBD Binding Properties of Neutralizing Antibodies Against SARS-CoV-2 Variants of Concern. Frontiers in Immunology, 12. https://doi.org/10.3389/fimmu.2021.691715

Dodero-Rojas, E., Onuchic, J. N., & Whitford, P. C. (2021a). Sterically confined rearrangements of sars-cov-2 spike protein control cell invasion. *ELife*, *10*. https://doi.org/10.7554/eLife.70362

Dodero-Rojas, E., Onuchic, J. N., & Whitford, P. C. (2021b). Sterically confined rearrangements of sars-cov-2 spike protein control cell invasion. *ELife*, *10*. https://doi.org/10.7554/eLife.70362

Dokainish, H. M., Re, S., Mori, T., Kobayashi, C., Jung, J., & Sugita, Y. (2022). The inherent flexibility of receptor binding domains in SARS-CoV- 2 spike protein. ELife, 11. https://doi.org/10.7554/eLife.75720

106

Du, L., Yang, Y., & Zhang, X. (2021). Neutralizing antibodies for the prevention and treatment of COVID-19. *Cellular and Molecular Immunology*, *18*(10), 2293–2306. https://doi.org/10.1038/s41423-021-00752-2

Dubochet, J., Adrian, M., Lepault, J., & McDowall, A. W. (1985). Emerging techniques: Cryo-electron microscopy of vitrified biological specimens. Trends in Biochemical Sciences, 10(4), 143–146. https://doi.org/10.1016/0968-0004(85)90150-1

Fedry, J., Hurdiss, D. L., Wang, C., Li, W., Obal, G., Drulyte, I., Du, W., Howes, S. C., van Kuppeveld, F. J. M., Förster, F., & Bosch, B. J. (2021). Structural insights into the cross-neutralization of SARS-CoV and SARS-CoV-2 by the human monoclonal antibody 47D11. *Science Advances*, *7*(23), 44–47. https://doi.org/10.1126/sciadv.abf5632

Gobeil, S. M. C., Henderson, R., Stalls, V., Janowska, K., Huang, X., May, A., Speakman, M., Beaudoin, E., Manne, K., Li, D., Parks, R., Barr, M., Deyton, M., Martin, M., Mansouri, K., Edwards, R. J., Eaton, A., Montefiori, D. C., Sempowski, G. D., … Acharya, P. (2022). Structural diversity of the SARS-CoV-2 Omicron spike. *Molecular Cell*, *82*(11), 2050-2068.e6. https://doi.org/10.1016/j.molcel.2022.03.028

Gobeil, S. M. C., Janowska, K., McDowell, S., Mansouri, K., Parks, R., Stalls, V., Kopp, M. F., Manne, K., Li, D., Wiehe, K., Saunders, K. O., Edwards, R. J., Korber, B., Haynes, B. F., Henderson, R., & Acharya, P. (2021). Effect of natural mutations of SARS-CoV-2 on spike structure, conformation, and antigenicity. *Science*, *373*(6555). https://doi.org/10.1126/science.abi6226

Harvey, W. T., Carabelli, A. M., Jackson, B., Gupta, R. K., Thomson, E. C., Harrison, E. M., Ludden, C., Reeve, R., Rambaut, A., Peacock, S. J., & Robertson, D. L. (2021). SARS-CoV-2 variants, spike mutations and immune escape. In *Nature Reviews Microbiology* (Vol. 19, Issue 7, pp. 409–424). Nature Research. https://doi.org/10.1038/s41579-021-00573-0

Hsieh, C. L., Goldsmith, J. A., Schaub, J. M., DiVenere, A. M., Kuo, H. C., Javanmardi, K., Le, K. C., Wrapp, D., Lee, A. G., Liu, Y., Chou, C. W., Byrne, P. O., Hjorth, C. K., Johnson, N. V., Ludes-Meyers, J., Nguyen, A. W., Park, J., Wang, N., Amengor, D., … McLellan, J. S. (2020). Structure-based design of prefusion-stabilized SARS-CoV-2 spikes. Science, 369(6509), 1501–1505. https://doi.org/10.1126/SCIENCE.ABD0826

Hsieh, C., Goldsmith, J. A., Schaub, J. M., Divenere, A. M., Kuo, H., Javanmardi, K., Le, K. C., Wrapp, D., Lee, A. G., Liu, Y., Chou, C., Byrne, P. O., Hjorth, C. K., Johnson, N. V, Ludes-meyers, J., Nguyen, A. W., Park, J., Wang, N., Amengor, D., … Mclellan, J. S. (2020). *Structure-based design of prefusion-stabilized SARS-CoV-2 spikes*. *1505*(September), 1501–1505.

Huang, Y., Long, Y., Li, S., Lin, T., Wu, J., Zhang, Y., & Lin, Y. (2018). Investigation on the processing and improving the cleavage efficiency of furin cleavage sites in Pichia pastoris. Microbial Cell Factories, 17(1). https://doi.org/10.1186/s12934-018-1020-x

Hussein, H. A. M., Thabet, A. A., Wardany, A. A., El-Adly, A. M., Ali, M., Hassan, M. E. A., Abdeldayem, M. A. B., Mohamed, A. R. M. A., Sobhy, A., El-Mokhtar, M. A., Afifi, M. M., Fathy, S. M., & Sultan, S. (2024). SARS-CoV-2 outbreak: role of viral proteins and genomic diversity in virus infection and

COVID-19 progression. In Virology Journal (Vol. 21, Issue 1). BioMed Central Ltd. https://doi.org/10.1186/s12985-024-02342-w

Ives, C. M., Nguyen, L., Fogarty, C. A., Harbison, A. M., Durocher, Y., Klassen, J., & Fadda, E. (2024). Role of N343 glycosylation on the SARS-CoV-2 S RBD structure and co-receptor binding across variants of concern. *ELife*, *13*, 1–39. https://doi.org/10.7554/eLife.95708

Jackson, C. B., Farzan, M., Chen, B., & Choe, H. (2022). Mechanisms of SARS-CoV-2 entry into cells. In *Nature Reviews Molecular Cell Biology* (Vol. 23, Issue 1, pp. 3–20). Nature Research. https://doi.org/10.1038/s41580-021-00418-x

Kadam, S. B., Sukhramani, G. S., Bishnoi, P., Pable, A. A., & Barvkar, V. T. (2021). SARS-CoV-2, the pandemic coronavirus: Molecular and structural insights. *Journal of Basic Microbiology*, *61*(3), 180–202. https://doi.org/10.1002/jobm.202000537

Klinakis, A., Cournia, Z., & Rampias, T. (2021). N-terminal domain mutations of the spike protein are structurally implicated in epitope recognition in emerging SARS-CoV-2 strains. *Computational and Structural Biotechnology Journal*, *19*, 5556–5567. https://doi.org/10.1016/j.csbj.2021.10.004

Krissinel, E., & Henrick, K. (2007). Inference of Macromolecular Assemblies from Crystalline State. Journal of Molecular Biology, 372(3), 774–797. https://doi.org/10.1016/j.jmb.2007.05.022

Kuba, K., Yamaguchi, T., & Penninger, J. M. (2021). Angiotensin-Converting Enzyme 2 (ACE2) in the Pathogenesis of ARDS in COVID-19. In *Frontiers*

in Immunology (Vol. 12). Frontiers Media S.A. https://doi.org/10.3389/fimmu.2021.732690

Kumar, S., Chandele, A., & Sharma, A. (2021). Current status of therapeutic monoclonal antibodies against SARS-CoV-2. *PLoS Pathogens*, *17*(9). https://doi.org/10.1371/journal.ppat.1009885

Lan, J., Ge, J., Yu, J., Shan, S., Zhou, H., Fan, S., Zhang, Q., Shi, X., Wang, Q., Zhang, L., & Wang, X. (2020a). Structure of the SARS-CoV-2 spike receptor-binding domain bound to the ACE2 receptor. *Nature*, *581*(7807), 215–220. https://doi.org/10.1038/s41586-020-2180-5

Lan, J., Ge, J., Yu, J., Shan, S., Zhou, H., Fan, S., Zhang, Q., Shi, X., Wang, Q., Zhang, L., & Wang, X. (2020b). Structure of the SARS-CoV-2 spike receptor-binding domain bound to the ACE2 receptor. *Nature*, *581*(7807), 215–220. https://doi.org/10.1038/s41586-020-2180-5

Le, K., Kannappan, S., Kim, T., Lee, J. H., Lee, H. R., & Kim, K. K. (2023). Structural understanding of SARS-CoV-2 virus entry to host cells. In *Frontiers in Molecular Biosciences* (Vol. 10). Frontiers Media SA. https://doi.org/10.3389/fmolb.2023.1288686

Li, X., Mi, Z., Liu, Z., & Rong, P. (2024). SARS-CoV-2: pathogenesis, therapeutics, variants, and vaccines. In *Frontiers in Microbiology* (Vol. 15). Frontiers Media SA. https://doi.org/10.3389/fmicb.2024.1334152

Li, Y., Shen, Y., Zhang, Y., & Yan, R. (2023). Structural Basis for the Enhanced Infectivity and Immune Evasion of Omicron Subvariants. *Viruses*, *15*(6). https://doi.org/10.3390/v15061398

110

Liu, H., Tian, Z., Yuan, S., & Zhou, S. (2023). Molecular mechanism study of the structural regulation of the N-terminal domain binding antibody on the receptor binding domain of SARS-CoV-2. *Physical Chemistry Chemical Physics*, 15237–15247. https://doi.org/10.1039/d3cp01378b

Manjunath, R., Gaonkar, S. L., Saleh, E. A. M., & Husain, K. (2022). A comprehensive review on Covid-19 Omicron (B.1.1.529) variant. In *Saudi Journal of Biological Sciences* (Vol. 29, Issue 9). Elsevier B.V. https://doi.org/10.1016/j.sjbs.2022.103372

Mannar, D., Saville, J. W., Zhu, X., Srivastava, S. S., Berezuk, A. M., Tuttle, K. S., Citlali Marquez, A., Sekirov, I., & Subramaniam, S. (n.d.). *SARS-CoV-2 Omicron variant: Antibody evasion and cryo-EM structure of spike protein-ACE2 complex*. https://www.science.org

Markov, P. V., Ghafari, M., Beer, M., Lythgoe, K., Simmonds, P., Stilianakis, N. I., & Katzourakis, A. (2023). The evolution of SARS-CoV-2. In *Nature Reviews Microbiology* (Vol. 21, Issue 6, pp. 361–379). Nature Research. https://doi.org/10.1038/s41579-023-00878-2

McGinnis, S., & Madden, T. L. (2004). BLAST: At the core of a powerful and diverse set of sequence analysis tools. Nucleic Acids Research, 32(WEB SERVER ISS.). https://doi.org/10.1093/nar/gkh435

Miner, J. C., Fenimore, P. W., Fischer, W. M., McMahon, B. H., Sanbonmatsu, K. Y., & Tung, C. S. (2022). Integrative structural studies of the SARS-CoV-2 spike protein during the fusion process (2022). *Current Research in Structural Biology*, *4*, 220–230. https://doi.org/10.1016/j.crstbi.2022.06.004

Nayak, T., De, D., & Dhal, P. K. (2020). *Since January 2020 Elsevier has created a COVID-19 resource centre with free information in English and Mandarin on the novel coronavirus COVID- 19 . The COVID-19 resource centre is hosted on Elsevier Connect , the company ' s public news and information . January*.

Papa, G., Mallery, D. L., Albecka, A., Welch, L. G., Cattin-Ortolá, J., Luptak, J., Paul, D., McMahon, H. T., Goodfellow, I. G., Carter, A., Munro, S., & James, L. C. (2021). Furin cleavage of SARS-CoV-2 Spike promotes but is not essential for infection and cell-cell fusion. *PLoS Pathogens*, *17*(1). https://doi.org/10.1371/journal.ppat.1009246

Patel, V. B., Zhong, J. C., Grant, M. B., & Oudit, G. Y. (2016). Role of the ACE2/angiotensin 1-7 axis of the renin-angiotensin system in heart failure. In *Circulation Research* (Vol. 118, Issue 8, pp. 1313–1326). Lippincott Williams and Wilkins. https://doi.org/10.1161/CIRCRESAHA.116.307708

Petersen, O. H., Gerasimenko, O. V., & Gerasimenko, J. V. (2020). Endocytic uptake of SARS-CoV-2: The critical roles of pH, Ca2+, and NAADP. *Function*, *1*(1). https://doi.org/10.1093/function/zqaa003

Pipitò, L., Rujan, R. M., Reynolds, C. A., & Deganutti, G. (2022). Molecular dynamics studies reveal structural and functional features of the SARS-CoV-2 spike protein. In BioEssays (Vol. 44, Issue 9). John Wiley and Sons Inc. https://doi.org/10.1002/bies.202200060

Pondé, R. A. A. (2022). Physicochemical effect of the N501Y, E484K/Q, K417N/T, L452R and T478K mutations on the SARS-CoV-2 spike protein RBD and its influence on agent fitness and on attributes developed by emerging variants of

concern. In *Virology* (Vol. 572, pp. 44–54). Academic Press Inc. https://doi.org/10.1016/j.virol.2022.05.003

Saceleanu, V., Moreanu, M. S., Covache-Busuioc, R. A., Mohan, A. G., & Ciurea, A. V. (2022). SARS-COV-2 – the pandemic of the XXI century, clinical manifestations – neurological implications. *Journal of Medicine and Life*, *15*(3), 319–327. https://doi.org/10.25122/jml-2020-0151

Safarzadeh Kozani, P., Safarzadeh Kozani, P., & Rahbarizadeh, F. (2024). Humanization of the antigen-recognition domain does not impinge on the antigen-binding, cytokine secretion, and antitumor reactivity of humanized nanobody-based CD19-redirected CAR-T cells. Journal of Translational Medicine, 22(1). https://doi.org/10.1186/s12967-024-05461-8

Stalls, V., Lindenberger, J., Gobeil, S. M. C., Henderson, R., Parks, R., Barr, M., Deyton, M., Martin, M., Janowska, K., Huang, X., May, A., Speakman, M., Beaudoin, E., Kraft, B., Lu, X., Edwards, R. J., Eaton, A., Montefiori, D. C., Williams, W. B., … Acharya, P. (2022). Cryo-EM structures of SARS-CoV-2 Omicron BA.2 spike. Cell Reports, 39(13). https://doi.org/10.1016/j.celrep.2022.111009

Stalls, V., Lindenberger, J., Gobeil, S. M. C., Henderson, R., Parks, R., Barr, M., Deyton, M., Martin, M., Janowska, K., Huang, X., May, A., Speakman, M., Beaudoin, E., Kraft, B., Lu, X., Edwards, R. J., Eaton, A., Montefiori, D. C., Williams, W. B., … Acharya, P. (2022). Cryo-EM structures of SARS-CoV-2 Omicron BA.2 spike. *Cell Reports*, *39*(13). https://doi.org/10.1016/j.celrep.2022.111009

Tam, D., Lorenzo-leal, A. C., & Ricardo, L. (2023). *Targeting SARS-CoV-2 Non-Structural Proteins*. 1–28.

Tegally, H., Moir, M., Everatt, J., Giovanetti, M., Scheepers, C., Wilkinson, E., Subramoney, K., Makatini, Z., Moyo, S., Amoako, D. G., Baxter, C., Althaus, C. L., Anyaneji, U. J., Kekana, D., Viana, R., Giandhari, J., Lessells, R. J., Maponga, T., Maruapula, D., … de Oliveira, T. (2022). Emergence of SARS-CoV-2 Omicron lineages BA.4 and BA.5 in South Africa. *Nature Medicine*, *28*(9), 1785–1790. https://doi.org/10.1038/s41591-022-01911-2

Tuvi-Arad, I., & Shalit, Y. (2023). The SARS-CoV-2 spike protein structure: a symmetry tale on distortion trail. *Physical Chemistry Chemical Physics*, *25*(20), 14430–14439. https://doi.org/10.1039/d3cp00163f

Uwamino, Y., Yokoyama, T., Shimura, T., Nishimura, T., Sato, Y., Wakui, M., Kosaki, K., Hasegawa, N., & Murata, M. (2022). The effect of the E484K mutation of SARS-CoV-2 on the neutralizing activity of antibodies from BNT162b2 vaccinated individuals. *Vaccine*, *40*(13), 1928–1931. https://doi.org/10.1016/j.vaccine.2022.02.047

Valério, M., Borges-Araújo, L., Melo, M. N., Lousa, D., & Soares, C. M. (2022). SARS-CoV-2 variants impact RBD conformational dynamics and ACE2 accessibility. Frontiers in Medical Technology, 4. https://doi.org/10.3389/fmedt.2022.1009451

Walls, A. C., Park, Y. J., Tortorici, M. A., Wall, A., McGuire, A. T., & Veesler, D. (2020a). Structure, Function, and Antigenicity of the SARS-CoV-2 Spike Glycoprotein. *Cell*, *181*(2), 281-292.e6. https://doi.org/10.1016/j.cell.2020.02.058

Walls, A. C., Park, Y. J., Tortorici, M. A., Wall, A., McGuire, A. T., & Veesler, D. (2020b). Structure, function and antigenicity of the SARS-CoV-2 spike glycoprotein. *BioRxiv*, *January*. https://doi.org/10.1101/2020.02.19.956581

Walls, A. C., Tortorici, M. A., Frenz, B., Snijder, J., Li, W., Rey, F. A., DiMaio, F., Bosch, B. J., & Veesler, D. (2016). Glycan shield and epitope masking of a coronavirus spike protein observed by cryo-electron microscopy. *Nature Structural and Molecular Biology*, *23*(10), 899–905. https://doi.org/10.1038/nsmb.3293

Wang, M. Y., Zhao, R., Gao, L. J., Gao, X. F., Wang, D. P., & Cao, J. M. (2020). SARS-CoV-2: Structure, Biology, and Structure-Based Therapeutics Development. *Frontiers in Cellular and Infection Microbiology*, *10*(November), 1–17. https://doi.org/10.3389/fcimb.2020.587269

Wang, Q., Guo, Y., Iketani, S., Nair, M. S., Li, Z., Mohri, H., Wang, M., Yu, J., Bowen, A. D., Chang, J. Y., Shah, J. G., Nguyen, N., Chen, Z., Meyers, K., Yin, M. T., Sobieszczyk, M. E., Sheng, Z., Huang, Y., Liu, L., & Ho, D. D. (2022). Antibody evasion by SARS-CoV-2 Omicron subvariants BA.2.12.1, BA.4 and BA.5. *Nature*, *608*(7923), 603–608. https://doi.org/10.1038/s41586-022-05053-w

Wang, Y., Liu, C., Zhang, C., Wang, Y., Hong, Q., Xu, S., Li, Z., Yang, Y., Huang, Z., & Cong, Y. (2022). Structural basis for SARS-CoV-2 Delta variant recognition of ACE2 receptor and broadly neutralizing antibodies. *Nature Communications*, *13*(1). https://doi.org/10.1038/s41467-022-28528-w

Wrapp, D., Wang, N., Corbett, K. S., Goldsmith, J. A., Hsieh, C. L., Abiona, O., Graham, B. S., & McLellan, J. S. (2020). Cryo-EM structure of the 2019-nCoV

115

spike in the prefusion conformation. *Science*, *367*(6483), 1260–1263. https://doi.org/10.1126/science.aax0902

Wu, H., Nie, Y., Huse, W. D., & Watkins, J. D. (1999). Humanization of a Murine Monoclonal Antibody by Simultaneous Optimization of Framework and CDR Residues. http://www.idealibrary.com

Xu, A., Hong, B., Lou, F., Wang, S., Li, W., Shafqat, A., An, X., Zhao, Y., Song, L., Tong, Y., & Fan, H. (2022). Sub-lineages of the SARS-CoV-2 Omicron variants: Characteristics and prevention. In *MedComm* (Vol. 3, Issue 3). John Wiley and Sons Inc. https://doi.org/10.1002/mco2.172

Yan, R., Zhang, Y., Li, Y., Xia, L., Guo, Y., & Zhou, Q. (2020). Structural basis for the recognition of SARS-CoV-2 by full-length human ACE2. In *Science* (Vol. 367).

Zekri, L., Ruetalo, N., Christie, M., Walker, C., Manz, T., Rammensee, H. G., Salih, H. R., Schindler, M., & Jung, G. (2023). Novel ACE2 fusion protein with adapting activity against SARS-CoV-2 variants in vitro. *Frontiers in Immunology*, *14*. https://doi.org/10.3389/fimmu.2023.1112505

Zhang, Q., Xiang, R., Huo, S., Zhou, Y., Jiang, S., Wang, Q., & Yu, F. (2021). Molecular mechanism of interaction between SARS-CoV-2 and host cells and interventional therapy. In Signal Transduction and Targeted Therapy (Vol. 6, Issue 1). Springer Nature. https://doi.org/10.1038/s41392-021-00653-w

Zhu, Y., Feng, F., Hu, G., Wang, Y., Yu, Y., Zhu, Y., Xu, W., Cai, X., Sun, Z., Han, W., Ye, R., Chen, H., Ding, Q., Qu, D., Xie, Y., Yuan, Z., & Zhang, R. (n.d.). *The S1/S2 boundary of SARS-CoV-2 spike protein modulates cell 1 entry pathways and transmission 2 3*. https://doi.org/10.1101/2020.08.25.266775

Zhu, Y., Feng, F., Hu, G., Wang, Y., Yu, Y., Zhu, Y., Xu, W., Cai, X., Sun, Z., Han, W., Ye, R., Qu, D., Ding, Q., Huang, X., Chen, H., Xu, W., Xie, Y., Cai, Q., Yuan, Z., & Zhang, R. (2021). A genome-wide CRISPR screen identifies host factors that regulate SARS-CoV-2 entry. *Nature Communications*, *12*(1). https://doi.org/10.1038/s41467-021-21213-4

List of publications

-       **Costanzo, A**.; Fata, F.; Freda, I.; De Sciscio, M. L.; Gugole, E.; Bulfaro, G.; Di Renzo, M.; Barbizzi, L.; Exertier, C.; Parisi, G.; D'Abramo, M.; Vallone, B.; Savino, C.; Montemiglio, L. C. Binding of Steroid Substrates Reveals the Key to the Productive Transition of the Cytochrome P450 OleP. Structure 2024.

-       De Sciscio, M. L.; Nardi, A. N.; Parisi, G.; Bulfaro, G.; **Costanzo, A**.; Gugole, E.; Exertier, C.; Freda, I.; Savino, C.; Vallone, B.; Montemiglio, L. C.; D'Abramo, M. Effect of Salts on the Conformational Dynamics of the Cytochrome P450 OleP. Molecules 2023, 28 (2), 832.

Acknowledgements

In conclusion, it has been a true pleasure to share my PhD journey with my research group colleagues: Giovanni Bulfaro, Cècile Exertier, Ida Freda, Elena Gugole, Francesca Fata and Arianna Lardieri. I am deeply grateful for supporting me and putting up with me over these years.